

Material Transport in Oceanic Gyres. Part III: Randomized Stochastic Models

PAVEL S. BERLOFF

Woods Hole Oceanographic Institution, Woods Hole, Massachusetts

JAMES C. MCWILLIAMS

Institute of Geophysics and Planetary Physics, University of California, Los Angeles, Los Angeles, California

(Manuscript received 3 January 2002, in final form 18 November 2002)

ABSTRACT

Transport models are required for simulating the subgrid-scale transport by mesoscale eddies, which are typically not resolved in coarse-grid representations of the ocean circulation. Here, a new transport model from the class of stochastic models is formulated and its performance is tested against an eddy-resolving solution of the ocean circulation. The new approach overcomes drawbacks of the standard Markov models by broadening the range of simulated motions and by allowing transitions from one type of motion to another. The stochastic transport models yield random motion of individual passive particles, and the probability density function of the particle population may be interpreted as the concentration of a passive tracer. The models are developed for simulating observed transports of material by turbulent flows in the presence of coherent fluid structures, and they use only few internal parameters characterizing particular type of turbulence. The idea of stochastic randomization is introduced in the hierarchy of inhomogeneous and nonstationary stochastic models, and it is illustrated with the first kinematic-time parameter in the second-order Markov model. The principal property of the randomized stochastic hierarchy is its capability to simulate a broad range of intermediate-time, nondiffusive, single-particle dispersion behaviors involving a variety of timescales and length scales. This property is missing in the standard, nonrandomized hierarchy of Markov models which, as shown in a previous study, introduces errors in Lagrangian velocity correlation function and the corresponding material spreading process. The randomization implies that the parameter is represented by a probability distribution rather than a fixed average value. The probability distribution represents different populations of mesoscale fluctuations coexisting within a geographical region. The randomization effects are first studied in a homogeneous situation. Then, the performance of the inhomogeneous stochastic model is tested against passive tracer transport simulated by the fluid-dynamic, eddy-resolving ocean model. It is shown that the randomized model performs systematically better than the nonrandomized one, although only modestly so in some transport measures. Also, systematic differences are found between the direct solution of the stochastic model and the corresponding diffusion process with the eddy diffusivity estimated from the stochastic model. A local algorithm is proposed for estimating all the model parameters.

1. Introduction

Material transport in the ocean is strongly influenced by the internal oceanic factors: boundaries, large-scale time-mean currents, broad range of coherent mesoscale and large-scale transient patterns, and geographical inhomogeneity of the underlying dynamic processes. The common strategy for understanding the oceanic transport consists of measuring Lagrangian transport properties (by tracking surface drifters and neutrally buoyant floats and by measuring concentrations of various chemical tracers) and formulating more simple than the fluid-dynamic equations transport models that simulate these properties. The transport models are characterized by

mathematical formalism and internal parameters; therefore, they are parameterizations of the physical transport. Each transport model implies algorithms for estimating its parameters from the statistical properties of the ocean observations. Further progress is achieved by inferring the parameters from rough characteristics of large-scale currents (i.e., without more detailed statistics of the flow). First, the transport models advance fundamental knowledge, and, second, they are applied in fluid-dynamic, coarse-grid, numerical ocean general circulation models (OGCMs) as parameterizations of the fluxes induced by unresolved mesoscale eddies.

Here, the focus is on the transport models that simulate ensembles of the Lagrangian trajectories. This paper deals with the standard hierarchy of *stochastic* transport models and further advances it by incorporating statistical distributions and random, rather than fixed, values of the internal parameters. The randomized trans-

Corresponding author address: Pavel S. Berloff, Woods Hole Oceanographic Institution, MS#29, Woods Hole, MA 02543.
E-mail: pberloff@whoi.edu

port models gain the capability to simulate observed broad variety of float trajectories, rather than sets of trajectories with properties narrowly grouped around the average behavior. The generalization idea is illustrated by the second-order model from the hierarchy, that is, the Markov-2 model, and the first kinematic-time parameter. The new transport model is tested against both the corresponding fluid-dynamic and the nonrandomized solutions.

In the introduction, the motivations are explained, the problem is posed, and the background is briefly described. In section 2 the hierarchy of stochastic transport models is presented. Some properties of the fluid-dynamic reference solution are described in section 3. Section 4 studies basic properties of the homogeneous, stationary, and unbounded, randomized transport model. The inhomogeneous and laterally bounded randomized model is tested against the fluid-dynamic solution, and a closure that relates the transport model parameters and the time-mean flow characteristics is examined in section 5. Conclusions and discussion follow in section 6.

a. Motivations of the randomization

The main motivation is to improve performance of the standard Markov models. These models simulate intermediate-time subdiffusive material spreading process only together with exaggerating oscillations of the single-particle dispersion function (Berloff and McWilliams 2002, hereinafter BM). The physical interpretation of that is simple: the real turbulence is populated by very different dynamical species (e.g., different types of coherent vortices, planetary waves, and transient jets) with distinct kinematic properties, but a high-order Markov model represents all the dynamical species in terms of just a single, average statistical population described by single-valued parameters. In general, material transport by the average population is not equal to the average transport by the ensemble of distinct dynamical populations,¹ and the standard Markov-model approach narrows the range of properties of simulated particle trajectories for a given intermediate-time material spreading rate. Our preliminary results find another drawback of the standard approach: the two- and multiparticle extensions of the Markov models, which simulate not only the spreading but also the mixing process defined in terms of the relative dispersion (Piterbarg 2001), strongly underestimate the mixing rates because of the exaggerated single-particle dispersion oscillations. The approach taken in this paper offers a solution

¹ This idea, in a more simple form, has been already introduced in the form of a pair of distinct populations in a one-dimensional inhomogeneous (e.g., Luhar et al. 1996) and a two-dimensional homogeneous Markov-1 models (Pasquero et al. 2001); and in the form of time-dependent spin statistics for the homogeneous Markov-1 model (Reynolds 2002). However, none of these results account for particle transitions between the populations.

to all these problems by introducing several Lagrangian particle populations with distinct properties and by allowing transition from one population to another. Physically, the approach accounts for particles migrating from one type of mesoscale fluctuation to another; and, mathematically, this is expressed in terms of the parameter randomization.

b. Statement of the problem

Results of this paper are a part of a long-term strategy aimed at solving the problem of transport by ocean mesoscale eddies. The strategy consists of several aspects:

- 1) creation of skillful transport models, with rigorous testing against ocean observations and fluid-dynamic eddy-resolving simulations of the ocean circulation;
- 2) implementation of transport models as subgrid-scale parameterizations in OGCMs;
- 3) closures that simply relate the transport model parameters to the coarse-grid dynamic fields, which are explicitly resolved in OGCMs.

This paper advances aspect 1 in the framework of stochastic transport models and explores aspects 2 and 3 for an idealized quasigeostrophic (QG) ocean model. The challenge is to incorporate in the stochastic transport models more complete statistical information about the turbulence, without falling into excessive complexity.

A common transport model that represents and parameterizes the passive-tracer, mesoscale, eddy-induced transport in coarse-grid OGCMs is *diffusion* (also called turbulent eddy diffusion: Taylor 1921). The diffusion process represents the large-time asymptotic behavior of the single-particle dispersion in homogeneous and stationary turbulence in an unbounded domain. The corresponding evolution of the tracer concentration, $c(t, \mathbf{x})$, is governed by the classical advection–diffusion equation,

$$\frac{\partial c}{\partial t} + \bar{\mathbf{u}} \cdot \nabla c = \nabla \cdot (\mathbf{K} \cdot \nabla c), \quad (1)$$

where $\bar{\mathbf{u}}$ is the large-scale, explicitly resolved advective velocity vector, and \mathbf{K} is the diffusivity tensor coefficient. In the ocean and atmosphere, on the most energetic length scales, the values of \mathbf{K} are larger by many orders of magnitude than the molecular diffusivity of water. The widespread use of (1) is due to its simplicity, elegance, and capability of simulating transport characterized by single-particle dispersion that is a linear function of time. On the other hand, (1) is based on the assumption of rapid Lagrangian velocity decorrelation (i.e., a rapid memory loss following Lagrangian particles), which is not accurate in the presence of long-living coherent structures, such as oceanic mesoscale eddies.

A class of transport models that, to some degree, accounts for the presence of coherent structures in the

flow is the stochastic model hierarchy based on random Markov processes (BM). In this approach the locally averaged concentration of particles, that is, the probability density function (PDF) of particle positions, is proportional to the tracer concentration, $c(t, \mathbf{x})$. However, the stochastic models simulate not only $c(t, \mathbf{x})$, but also Lagrangian particle trajectories and material fluxes between any locations. In this paper the stochastic hierarchy formalism is advanced toward the new class of randomized Markov (RM) models. In order to test the transport models, the focus is on the midlatitude oceanic gyres, such as in the North Pacific, and North and South Atlantic.² The standard solution of the transport in oceanic gyres is computed with an idealized fluid-dynamic circulation model; and the simple transport model has to simulate it with (ultimately, just a few) parameters estimated from the fluid-dynamic solution.

The main assumptions in this study are the following.

- 1) The fluid motion is two-dimensional within each isopycnal fluid layer.
- 2) The transport induced by fluid-dynamically unresolved submesoscale eddies is negligible.
- 3) The tracer is dynamically passive.
- 4) The tracer evolution is simulated by randomly moving particles that are not correlated with each other.
- 5) The random forcing has a Gaussian (i.e., normal) distribution at each location. Discussion on how to extend the theory and overcome the assumptions is in the end of section 6.

The primary goal of this paper is to find a transport model formalism accounting for the broad variety of different Lagrangian motions that are simultaneously present in oceanic mesoscale turbulence. This goal is achieved by incorporating realistic distributions of the first kinematic-time parameter in the second-order stochastic transport model. Physically, different values of the parameter characterize kinematic properties of distinct dynamical populations of coherent fluctuations inside the turbulence. This idea can be straightforwardly extended to all parameters of any transport model from the standard stochastic model hierarchy, and the corresponding models from the new family are called the randomized Markov models. Here, the effect of the randomization is analyzed both in a homogeneous situation and in the inhomogeneous oceanic gyres.

With respect to Lagrangian float data for estimating transport model parameters, in addition to the standard statistical issues (Griffa et al. 1995), the following concerns arise.

Increased data efficiency. It is important to ensure that the observation float data requirements for the RM models are not larger than for the standard

nonrandomized Markov models. As shown, improved performance of the RM models is achieved by better utilization of the information contained in the data, rather than by expanding the datasets.

Any type of measurements. In the RM models, both Lagrangian and Eulerian ocean measurements may be used for estimating the parameters, but in practice Lagrangian measurements are often more efficient because of relatively low costs of floats. On the other hand, one has to remember that Lagrangian measurements introduce nonlocality and the associated uncertainty in parameter estimates.

Locality of the parameter estimates. The parameter estimate algorithms should be able to determine the parameters as locally in space and time as possible, and this is particularly acute requirement in locations where inhomogeneities of the transport properties are strong [e.g., in such places as western boundary currents (WBCs) with associated eastward jet extensions, other narrow and swift currents, coastal regions, flows over complex topography, regions of localized instabilities, and regions with enhanced local diabatic forcing]. For comparison, the traditional approach of estimating eddy diffusivity coefficients (section 1c) is nonlocal, because the estimates use nonlocal large-time asymptotic information contained in the Lagrangian integral time. When applying the RM models, a parameter estimation algorithm is proposed that satisfies the locality requirement.

There are two types of applications of the RM models presented here. The *direct* approach completely replaces the traditional advection–diffusion equation with an RM model—arguably, this is the most direct and accurate way to account for the presence of the coherent structures. The *interim* approach is simpler but it accounts for the presence of the coherent structures to a lesser degree. Here, the idea is to analyze the ocean data within the RM formalism, to estimate the eddy diffusivity parameter with the RM model, and to simulate the transport with the diffusion model characterized by this parameter. In this paper, both approaches are compared and their systematic differences are identified.

The RM approach allows one to locally estimate the Lagrangian integral time T_L , which is a fundamental transport property. The T_L is also estimated with alternative approaches: one of them is based on the flow fluctuation energy and enstrophy densities (Babiano et al. 1987), and the other relates T_L to the local baroclinic instability process (Visbeck et al. 1997; Stammer 1998). Finally, relationships, that is, closures, between the transport model parameters and the time-mean flow are looked for. However, the very existence of the universal closures is questionable because, as shown here, the transport parameters strongly depend on the structure and internal correlations of the turbulent eddies and, in turn, these properties are related to the time-mean cur-

² The theory can be used for other aspects of the ocean circulation and, in general, for various turbulent flows in the presence of organized coherent patterns.

rents in a very complex way. A closure would allow one to determine transport model parameters from coarse-grid OGCM flow characteristics that evolve in time, rather than to prescribe them beforehand.

c. Background

Material transport can be separated in two processes: spreading and mixing. The former is the propagation of material from its initial location (e.g., described by single-particle dispersion), and the latter is the disappearance of internal structure in an evolving patch of material (e.g., described by two-particle dispersion). On the fundamental level, nontrivialities of the spreading and mixing processes are related to long-time memory and long-range correlations associated with characteristic time- and length scales of fluctuations. More specifically, the spreading rate is related to velocity autocorrelations following Lagrangian trajectories; the mixing rate is related to spatial velocity correlations between neighboring particles. Most previous works are concerned with developing transport models that simulate spreading rather than mixing rates. A unified formalism for modeling both transport processes in the presence of coherent fluid structures is a matter for the future.

Modeling oceanic transport started with the idea (Taylor 1921) that mesoscale eddies disperse material (or, equivalently, passive tracer) as in the classical diffusion process. In this approach the eddy diffusivity, K , is estimated either as the linear slope of the single-particle dispersion function or as $K = \sigma T_L$, where σ is the velocity variance and T_L is the integral timescale of the Lagrangian velocity autocorrelation function, $R(\tau)$ (section 2b). The fundamental assumption made in the diffusion process is that Lagrangian velocities decorrelate instantaneously (as a consequence, the eddies are assumed to have infinitesimal correlation time- and lengthscales). This assumption is violated in the presence of coherent structures such as mesoscale eddies. Relaxing it requires alternative transport models. Also, the correctness of the diffusion model is undermined by the need to look for large-time asymptotic Lagrangian behavior in the presence of widespread ocean flow inhomogeneities.³ The combination of the inhomogeneities and float trajectories covering a large area typically yields spatially nonlocal and, therefore, incorrect eddy diffusivity estimates. This is a result of averaging data contributed by geographical regions with different transport properties. Commonly, the corresponding errors in large-scale transport simulations by the diffusion model are not known. Even the inhomogeneities themselves of

oceanic transport properties are poorly known.⁴ Another source of errors and biases in estimates of K is due to statistical uncertainty of separating contributions by the time-mean flow and fluctuations. This error also can be substantially reduced if K is estimated locally.

Substantial deviations from diffusive behavior and a large variety of intermediate-time dispersion behaviors are found in ocean measurements with Lagrangian floats (Freeland et al. 1975; Krauss and Böning 1987; Rupolo et al. 1996; LaCasce and Bower 2000). General ocean circulation (Figueroa and Olson 1994; Figueroa 1994; Bower and Lozier 1994) and 2D turbulence models (Babiano et al. 1987) also generate nondiffusive spreading behaviors due to persistent velocity correlations in organized flow patterns. BMB show that in most of the midlatitude ocean (and more so in its deep part) intermediate-time, subdiffusive (slow), single-particle dispersion behavior occurs due to long-time trapping of material by coherent structures such as vortices near the strong currents and planetary waves in the eastern part of the gyres. Intermediate-time, superdiffusive (fast), single-particle dispersion behavior is found in the central part of the subtropical gyre and near the lateral boundaries. The regions of sub- and superdiffusive behaviors correspond to the transport barriers and pathways, respectively. The works referenced here and many others suggest that the transport induced by mesoscale oceanic eddies requires a better model than eddy diffusion.

Other transport modeling approaches include stochastic models for the velocity gradient tensor, models in which concentration changes discontinuously at discrete times, and models with stochasticity in both velocity vector and dissipation rates (Pope 1994; Borgas and Sawford 1994). Another idea is to use a generalized advection–diffusion model that relates the transport to the time-lagged concentration gradient (Davis 1987), but it is relatively difficult to estimate the model parameters from the observations.

A powerful class of transport models is based on stochastic differential equations (SDEs) (e.g., Gardiner 1983; Sawford 1991; Pope 1994; Rodean 1996; for the oceanographic context, see Griffa 1996). The central idea of this approach is to represent some aspects of the turbulence variability as a simple random process and to simulate explicitly some important properties of the rest. As a matter of fact, the diffusion model is derived from the random-walk model that is the simplest stochastic process, which is based on random increments of the Lagrangian particle position. Beyond the random walk, there are more sophisticated stochastic transport models, united in a hierarchy, that introduce random

³ Observations show that the eddy timescales and length scales, as well as fluctuation energy density, vary greatly over the ocean (Lumpkin et al. 2002).

⁴ Eddy-resolving simulations of the ocean general circulation suggest that the inhomogeneities are of two kinds: eddy energy densities and single-particle dispersion rates (Berloff et al. 2002; hereinafter BMB). Both aspects vary strongly in some parts of the ocean; hence the eddy diffusivity is particularly ill-estimated there.

increments in SDEs governing high-order time derivatives of the particle position (BM). By restricting the random noise to higher derivatives and by explicitly solving for more aspects of the motion, these models account, to some degree, for the presence of coherent structures in turbulence and for the long-time Lagrangian velocity correlations associated with the coherence. The stochastic transport models satisfy the well-mixed condition (Thomson 1987) that ensures the correctness of the small-time behavior of the velocity distribution of particles spreading from a localized source, the compatibility of the stochastic model with Eulerian equations of motion, and the compatibility of forward and backward in time formulations of the models. If the constraint is satisfied, an important physical property is satisfied: a uniform distribution of tracer concentration remains uniform during adiabatic evolution.

Despite recent progress in stochastic transport models, this approach has many unsolved fundamental issues. The models have to be advanced so that they better simulate observed broad variety of Lagrangian time-scales and, therefore, the spreading process (this is the main focus of this paper). In particular, a drawback in the Markov model hierarchy is that, for a given average intermediate-time spreading rate, the models tend to exaggerate oscillations of the single-particle dispersion function because they do not account for the true range of different Lagrangian behaviors associated with different types of coherent mesoscale fluctuations. Another progress is required in testing the transport models against fluid-dynamic solutions in the realistic three-dimensional and nonstationary regimes. Intermittency (i.e., presence of nonnormal statistical distributions) of turbulence is common in the ocean (Bracco et al. 2000), and its transporting effect has to be represented in the models (Luhar et al. 1996; Maurizi and Lorenzani 2001; Pasquero et al. 2001). The most physical lateral boundary condition has to be found. Finally, flow fluctuations can cause a mean Lagrangian transport that is intrinsically nondiffusive (e.g., as in the Stokes drift of surface gravity waves), and to date no one has investigated how this behavior is modeled by the stochastic hierarchy.

Local internal parameters of a transport model represent local physics of the turbulence, and in general they are found from real ocean measurements. On the other hand, local physics of the turbulence can be a function of large-scale, time-mean flow characteristics. In this case, internal transport parameters can be related to the flow, and the relationship is referred to as a “closure.” The idea of parameterization is that of combining a transport model and its closure and adapting the combination for practical purposes. In the OGCM context, a closure is required between a theoretical model parameters and the coarse-grid flow characteristics (e.g., in the diffusion model: local eddy diffusivity as a function of local coarse-grid velocities). Eddy-resolving primitive equation models of oceanic gyres show weak

(but nonzero) correlation between the eddy fluxes and mean gradients of isopycnic thickness, potential vorticity, and temperature (Roberts and Marshall 2000), and there is evidence of a relationship between the eddy diffusivity and the local density stratification (Visbeck et al. 1997).

2. Hierarchy of Markov models

a. Formulation

In this section the general formulation is presented of the stochastic transport model hierarchy (see BM for details). The central idea of the theory is the following. Transport of a turbulent flow regime is simulated with a set of SDEs that govern motions of individual particles. The particle velocities contain both the time-mean and random components that correspond to the time-mean⁵ and fluctuating currents of the flow. A set of SDEs, together with internal parameters, boundary and initial conditions, and a time integration rule, constitute a stochastic transport model. No such model can simulate all aspects of the fluid dynamics, and here the goal is to simulate only some important statistical Lagrangian properties of the flow regime (e.g., single-particle dispersion). The transport model parameters are statistically estimated from Eulerian (i.e., at a given location) and/or Lagrangian (i.e., from Lagrangian float trajectories) observations, and one is required to make the estimates as local, both in space and time, as possible. The probability that the system of particles is in a certain state is given by the corresponding conditional (i.e., in Lagrangian phase space) PDF, $P_L(0, \mathbf{x} | t, \mathbf{x})$, and each model has a Fokker–Planck equation for the phase-space evolution of its P_L (Risken 1989). The tracer concentration is the phase-space projection of P_L obtained by integrating over all the state variables except \mathbf{x} —this indicates that transport represented by sets of Lagrangian trajectories contains, in general, much more information than the corresponding physical-space transport represented by tracer concentration.

The general form of a model from the hierarchy is

$$\begin{aligned} d\mathbf{f}_1 &= \mathbf{\Delta}_1(t, \mathbf{f}_1, \mathbf{f}_2)dt, \\ d\mathbf{f}_2 &= \mathbf{\Delta}_2(t, \mathbf{f}_1, \mathbf{f}_2, \mathbf{f}_3)dt, \\ &\vdots \\ d\mathbf{f}_N &= \mathbf{\Delta}_N(t, \mathbf{f}_1, \mathbf{f}_2, \dots, \mathbf{f}_N)dt + b_{ij}(t, \mathbf{f}_1)dW_j(t), \end{aligned} \quad (2)$$

where $(\mathbf{f}_1, \mathbf{f}_2, \dots, \mathbf{f}_n, \dots, \mathbf{f}_N)$ is the state vector of the system, and each element of it, \mathbf{f}_n , is a 2D physical-space vector ($i = 1, 2$ and $j = 1, 2$ are spatial coordinate indices), and summation is implied over a repeated index across a product of tensors.⁶ The variables \mathbf{f}_n cor-

⁵ Here, the time-mean flow represents the explicitly resolved large-scale circulation. In an OGCM it is to be replaced with the explicit coarse-grid fluid-dynamic solution.

⁶ Otherwise, F_{ii} denotes the i th diagonal component of \mathbf{F} .

respond to $\mathbf{x}, \mathbf{u}, \dot{\mathbf{u}}, \dots$, for $n = 1, 2, 3, \dots$. The Δ_n are deterministic functions; $d\mathbf{W}(t)$ is a random increment vector; and b_{ij} is the tensor amplitude multiplying the random increment vector. Random forcing enters only the last equation in (2), and it is an incremental Wiener process in each coordinate direction:

$$W_j(t) = \int_0^t \xi(s) ds. \quad (3)$$

The Wiener process is a continuous but nondifferentiable integral of a zero-mean, discontinuous, stationary, Gaussian, white-noise process, $\xi(t)$, with variance equal to the time step, dt . The relationship (3) is interpreted as $dW(t) = \xi(t) dt$ in (2). The boundary condition of choice for (2) is perfect reflection of particles from solid walls. Initial conditions for (2) are chosen randomly from the corresponding statistical distributions of the variables. The models are integrated in time with Ito calculus, except the time-mean advection term for which a fourth-order Runge–Kutta scheme is used. In a homogeneous, stationary situation and in an unbounded domain, each model from the hierarchy corresponds to a linear, stationary autoregressive process for the velocity fluctuation, and that allows for analytical solutions; otherwise the models are solved numerically.

The stochastic models use the following turbulence properties as the parameters. There are the variance tensors for the fluctuations of the velocity, \mathbf{u}' :

$$\sigma_{ij}(\mathbf{x}) = \overline{u'_i u'_j}; \quad (4)$$

acceleration, $\mathbf{g} = \dot{\mathbf{u}}'$:

$$\xi_{ij}(\mathbf{x}) = \overline{g_i g_j}; \quad (5)$$

and hyperacceleration, \mathbf{p} :

$$\zeta_{ij}(\mathbf{x}) = \overline{p_i p_j}, \quad (6)$$

where components of the hyperacceleration vector (BM) are defined as

$$p_i = \dot{u}'_i + \xi_{im}(\sigma^{-1})_{mj} u'_j, \quad (7)$$

and the overline operator, $\overline{f_i f_j}$, may be either an infinite- or a finite-time average; in the former situation it is assumed that the regime is stationary, and in the latter the stochastic model parameters are slowly varying functions of time. The physical meaning of p_i appears simple in the Markov-3 model: it is the linear combination of the rate of change of the acceleration and the average velocity fluctuation in its direction. In homogeneous and isotropic turbulence, each of (4), (5), and (6) corresponds to a single value of the variance.

Each stochastic model incorporates all properties of the models below it in the hierarchy. The simplest member of the hierarchy is referred to as the Markov-0 (or random-walk) model. It is equivalent (only in terms of tracer concentration evolution) to the advection–diffusion process (1), and it yields random displacements of

particle positions (appendix C). In the homogeneous and stationary case its governing equation is

$$dx_i = \bar{u}_i dt + (K^{1/2})_{ij} dW_j(t), \quad (8)$$

where $\mathbf{K} = K_{ij}$ is the diffusivity tensor coefficient. The Markov-1 governing equations for the particle coordinate and velocity fluctuation are

$$\begin{aligned} dx_i &= [\bar{u}_i(\mathbf{x}) + u'_i] dt, \\ du'_i &= [-\theta^{-1}(\mathbf{x})_{ij} u'_j + \tilde{a}_i(\mathbf{x}, \mathbf{u}')] dt + b_{ij}(\mathbf{x}) dW_j(t), \end{aligned} \quad (9)$$

where the first rhs term in the second equation represents a fading memory for velocity fluctuations; $\theta_{ij}(\mathbf{x})$ is the (Markov-1) fading-memory time tensor; and the drift correction term (for well-mixed condition) is

$$\begin{aligned} \tilde{a}_i &= \frac{1}{2} \frac{\partial \sigma_{ik}}{\partial x_k} - \frac{\sigma_{im}}{2} (\bar{u}_k + u'_k) \frac{\partial (\sigma^{-1})_{jm}}{\partial x_k} u'_j \\ &\quad - \frac{\sigma_{im}}{2} \frac{\partial (\sigma^{-1})_{mj}}{\partial x_k} u'_j u'_k. \end{aligned} \quad (10)$$

The Markov-1 random forcing amplitude is defined by

$$b_{ij} b_{jk} = 2\sigma_{ij}(\theta^{-1})_{jk}. \quad (11)$$

In addition to the continuous velocity, the Markov-2 model yields a continuous acceleration, $\dot{\mathbf{u}}$. Variable \mathbf{g} is called pseudoacceleration, and it is equal to $\dot{\mathbf{u}}'$ only in homogeneous and stationary situations (i.e., when $\tilde{\mathbf{a}} = 0$). The Markov-2 governing equations are

$$\begin{aligned} dx_i &= [\bar{u}_i(\mathbf{x}) + u'_i] dt, \\ du'_i &= g_i dt + \tilde{a}_i(\mathbf{x}, \mathbf{u}') dt, \\ dg_i &= [-\theta^{-1}(\mathbf{x})_{ij} g_j + \tilde{c}_i(\mathbf{x}, \mathbf{u}', \mathbf{g})] dt \\ &\quad + b_{ij}(\mathbf{x}) dW_j(t), \end{aligned} \quad (12)$$

where $\theta_{ij}(\mathbf{x})$ is the (Markov-2) fading-memory tensor; and the second drift-correction term is

$$\tilde{c}_i = -\xi_{im}(\sigma^{-1})_{mj} u'_j - \frac{\xi_{im}}{2} (\bar{u}_k - u'_k) \frac{\partial (\xi^{-1})_{jm}}{\partial x_k} g_j. \quad (13)$$

The Markov-2 random forcing amplitude is defined by

$$b_{ij} b_{jk} = 2\xi_{ij}(\theta^{-1})_{jk}. \quad (14)$$

b. Lagrangian properties

There are several Lagrangian properties that characterize some aspects of both turbulent flows and solutions of the models from the hierarchy, and only evolving PDF of particle ensembles contains the complete information on spreading process. In the oceanic gyres, a simple important property is the time-average, Lagrangian meridional flux of material. Another properties described below are more general.

The single-particle dispersion tensor (i.e., the mean-square particle displacement) is

$$D_{ij}[t, \mathbf{x}(0)] = \overline{[x_i(t) - x_i(0)][x_j(t) - x_j(0)]}, \quad (15)$$

where the overbar indicates an ensemble average over many particle trajectory realizations with the same initial position, $\mathbf{x}(0)$. Here, for simplicity, off-diagonal terms are neglected in all tensors (e.g., D_{ij} , R_{ij}) and the common geographical coordinates are used. This simplification does not change the fundamental issues but allows one to avoid many technical details.⁷ The main practical requirement to the transport models is to simulate observed $D(t)$. In the absence of boundaries and in the large-time limit, all the homogeneous and stationary Markov models asymptote to linearly growing $D(t)$ with a growth rate that depends on the parameters. In the ocean, intermediate-time evolution of $D(t)$ is very complex due to the presence of mesoscale eddies and geographical inhomogeneities. The homogeneous Markov models simulate relatively simple shapes of $D(t)$, but their skills increase with the order of the model (BM).

Another important transport properties are the Lagrangian velocity autocorrelation function,

$$R_{ij}(\tau) = \overline{u'_i(t)u'_j(t+\tau)}/(\overline{u'^2_i} \overline{u'^2_j})^{1/2}, \quad (16)$$

and its corresponding frequency power spectrum. Components of the Lagrangian time (tensor) are defined as

$$T_L = \int_0^\infty R(\tau) d\tau. \quad (17)$$

This quantity is nonlocal⁸ (except for homogeneous and stationary situation). In an inhomogeneous situation, the local value of T_L cannot be measured directly, but it can be found from a transport model with *locally* estimated parameters.

The $D(t)$ and $R(\tau)$ are connected by the relationships

$$\frac{d}{dt}D(t) = 2\sigma \int_0^t R(\tau) d\tau \quad \text{and} \quad (18)$$

$$D(t) = 2\sigma \int_0^t (t - \tau)R(\tau) d\tau. \quad (19)$$

From (18) it follows that in an unbounded domain⁹ $D(t)$ reaches a linear, that is, diffusive, regime after $R(\tau)$ decays to zero. In this limit, the diffusivity coefficient is defined as

$$K = \lim_{t \rightarrow \infty} \frac{d}{dt}D(t) = 2\sigma \int_0^t R(\tau) d\tau = 2\sigma T_L. \quad (20)$$

Since $D(t)$ is easily found from (19), we characterize the stochastic models in terms of $R(\tau)$. The Markov-0

$R(\tau)$ is a δ function, and therefore $D(t)$ is always in the linear regime uniquely characterized by the K . The zeroth degree of freedom, associated with the Markov-0 model, is the intensity of the velocity fluctuations that is expressed by σ , and hence by K . The homogeneous and stationary Markov-1 model in an unbounded domain is characterized by the exponential decay of the velocity correlations:

$$R(\tau) = \exp(-\tau/\theta), \quad (21)$$

where θ is the fading-memory timescale. Here, the first degree of freedom is associated with monotonic decay of the velocity correlations. The Markov-2 $R(\tau)$ has the second degree of freedom associated with oscillations (e.g., when the particles circulate inside coherent eddies) on the timescale $T^{(1)}$:

$$R(\tau) = \exp\left(-\frac{\tau}{\theta}\right) \sin\left(\frac{2\pi}{T^{(1)}}\tau + F\right)(\sin F)^{-1}, \quad (22)$$

where the phase shift, F , is found from the equation:

$$\tan F = \frac{1 + \exp(-2/\theta)}{1 - \exp(-2/\theta)} \tan\left(\frac{2\pi}{T^{(1)}}\right) \quad (23)$$

(Box et al. 1994). In the Markov-3 model, there is the third degree of freedom associated with asymmetry of the $R(\tau)$ (e.g., when the particles circulate inside drifting coherent eddies). In the two-dimensional Markov models with mutually correlated velocity components, it is shown that for $N > 0$: the N th-order model can exhibit dispersive properties of the $(N + 1)$ th-order model, and that implies complex eigenvalues of the linear transformation matrix in the rhs of the corresponding stochastic equation (Borgas et al. 1997; Reynolds 2002). Such models are more physical but also more complex. The formalism presented in this paper can be and has to be generalized in this direction.

3. Fluid-dynamic solution

a. General properties

The setup of the fluid-dynamic model used to test the stochastic theory is the same as in BMB, but the Reynolds number is 5 times larger, the numerical grid resolution is finer, and the fluctuations are more developed and energetic (appendix A). In the fluid-dynamic model, the passive tracer transport is represented by ensembles of Lagrangian particles advected by the velocity solution field. The particle trajectory is obtained by solving the nonautonomous equation,

$$\frac{d\mathbf{x}(t)}{dt} = \mathbf{u}(t, \mathbf{x}), \quad \mathbf{x}(t_0) = \mathbf{X}, \quad t \geq t_0, \quad (24)$$

where $\mathbf{x}(t, \mathbf{X})$ is the position of the particle initialized at time t_0 in location \mathbf{X} ; and $\mathbf{u} = (u, v)$ is the nondivergent, geostrophic, horizontal velocity, which can be decomposed into the time-mean and fluctuation compo-

⁷ Where it is obvious, the subscripts are dropped for convenience [e.g., $D(t)$, $R(\tau)$].

⁸ The corresponding errors are recognized in the ocean float data analysis, but their quantification is problematic.

⁹ In a bounded domain $D(t)$ reaches a finite global maximum at $t = \infty$.

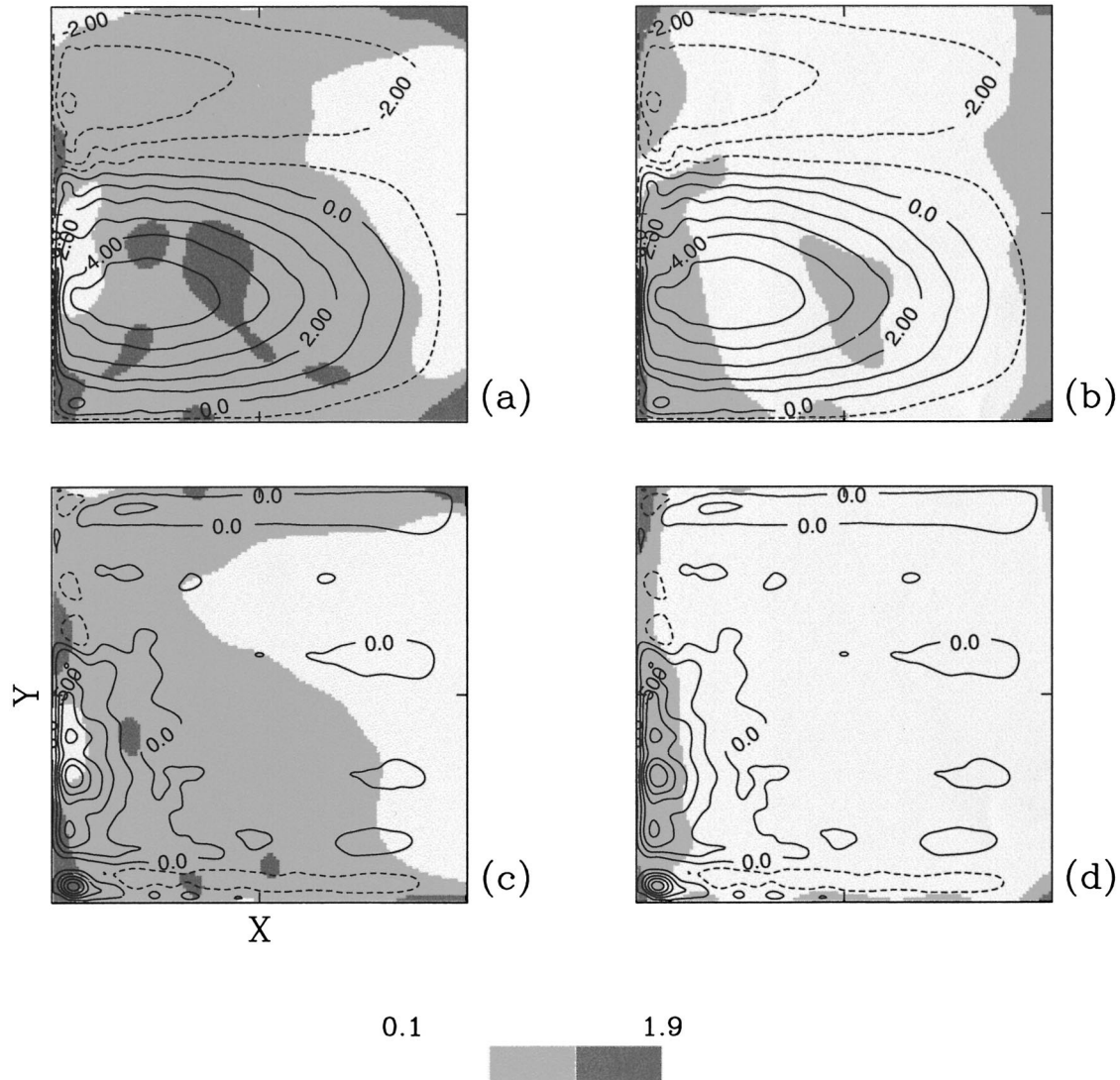


FIG. 1. Distributions of the (a), (c) zonal and (b), (d) meridional components of $\alpha_{ii}(x, y)$ from (27) in the (a), (b) upper and (c), (d) deep ocean. The time-mean velocity streamfunction is shown with (a), (b) contour interval (CI) = $10^4 \text{ m}^2 \text{ s}^{-1}$, and (c), (d) CI = $0.25 \times 10^4 \text{ m}^2 \text{ s}^{-1}$.

nents. To quantify the contribution from the fluctuation velocities, the single-particle dispersion is calculated as

$$D'_{ij}[t, \mathbf{x}(0)] = \overline{[x'_i(t) - x_i(0)][x'_j(t) - x_j(0)]}, \quad (25)$$

where $\mathbf{x}'(t)$ evolves by the local velocity fluctuation according to

$$\frac{d\mathbf{x}'(t)}{dt} = \mathbf{u}(t, \mathbf{x}) - \bar{\mathbf{u}}(\mathbf{x}). \quad (26)$$

In the absence of the time-mean flow, (25) reduces to (15). Over an intermediate-time interval, the single-particle dispersion is fitted to a power-law form,

$$D'_{ij}(t, x_{\text{bin}}, y_{\text{bin}}) \sim t^{\alpha_{ij}(x_{\text{bin}}, y_{\text{bin}}, z)}, \quad (27)$$

and then $\alpha_{ii}(x, y, z)$ is used to describe the Lagrangian transport rates under the assumption of local homoge-

neity (BMB). The α strongly varies over the basin, and a location is referred to as subdiffusive if $\alpha < 0.8$ (slow spreading), superdiffusive if $\alpha > 1.2$ (fast spreading), and approximately diffusive if $0.8 < \alpha < 1.2$ (exactly diffusive regime has $\alpha = 1$). The eastern part of the flow, that is away from the swift currents, is mostly subdiffusive; fast zonal spreading is found in the central part of the subtropical gyre, and fast meridional spreading is found in some parts of the WBCs (Fig. 1). In general, the spreading rates decrease with depth; they are enhanced along the lateral boundaries; and they have a pronounced local minimum near the WBC confluence zone. Overall, the α pattern is qualitatively similar to the one with 5 times smaller Re (BMB), but the transport rates are faster, and the time-mean flow contribution to the transport is different. We use the power laws as the

TABLE 1. The upper-ocean, mean intergyre fluxes (Sv; Sv $\equiv 10^6$ m³ s⁻¹) by time t (days). Abbreviations are FD: fluid-dynamic, RM2: randomized Markov-2, M2: Markov-2, and M0: Markov-0 (with K_{RM2}) solutions.

t	FD	RM-2	M-2	M-0
100	6.8	6.1	5.2	7.0
200	4.5	3.9	3.3	5.1
300	3.6	3.3	2.8	4.2
400	3.2	3.0	2.5	3.8
500	3.0	2.8	2.3	3.5

most straightforward and simple way to describe the fluid-dynamic transports in the oceanic gyres, but also they can be used for estimating parameters of the stochastic transport models. The main problem with the power laws is that they are nonlocal. This paper introduces the idea of the random parameters with the observed statistical distributions that, combined with information from the Eulerian velocity autocorrelations, allows one to avoid using the power laws in the parameter estimates.

In the oceanographic context, an important transport property, which we use to test the performance of the models, is the meridional intergyre flux of material. Across the intergyre boundary, by its definition as the time-mean streamline running from the western to the eastern boundary, there is no time-average Eulerian flux of material, but there is time-average Lagrangian flux. In the i th layer, the total, time-average, Lagrangian intergyre flux is

$$F_i^{(n,s)}(t) = \frac{V_i}{t} \int_0^L N_i^{(n,s)}(t, x) dx, \quad (28)$$

where $V_i = L^2 H_i / N$ is the fluid volume corresponding to each of N particles; $N_i^{(n,s)}(t, x)$ is the probability density of the first-time, intergyre boundary crossing; and the superscripts indicate whether the crossing is in the northward or southward direction. The intergyre fluxes are about twice larger than at 5 times smaller Re [$F_1(t)$ and $F_2(t)$ are shown in Tables 1 and 2, respectively]. Because of the integral mass conservation, $F^{(n)}(t) = F^{(s)}(t)$; but the crossing probability densities, $N^{(n)}(t, x)$ and $N^{(s)}(t, x)$, are generally not the same, thus indicating that there are locally nonzero net Lagrangian fluxes between the gyres (fluid-dynamic $N_i^{(n,s)}(t, x)$ are normalized by 1 and shown in Fig. 12).

b. First kinematic time

Ratios among the variance tensors (4)–(6) define two fundamental parameters that enter the Markov-2 and -3 models: the first and second kinematic-time tensors. By definition, the first kinematic time, $T^{(1)}$, is found from the relationship:

$$T_{ik}^{(1)} T_{kj}^{(1)} = \sigma_{ik}(\xi^{-1})_{kj}. \quad (29)$$

For simplicity pro tem, we neglect the nondiagonal el-

TABLE 2. As in Table 1 but for the deep ocean.

t	FD	RM-2	M-2	M-0
100	29.3	22.9	22.7	23.3
200	18.6	14.3	12.1	16.1
300	14.4	11.4	10.3	12.8
400	11.8	9.5	8.4	11.0
500	10.0	8.3	7.5	9.9

ements of $T_{ij}^{(1)}$, hence the important nondimensional parameter is

$$\beta^{(1)} = \frac{\theta}{T^{(1)}}, \quad (30)$$

for each coordinate direction. The second kinematic time, $T^{(2)}$, is found from

$$T_{ik}^{(2)} T_{kj}^{(2)} = \xi_{ik}(\xi^{-1})_{kj}. \quad (31)$$

The first kinematic time describes the average rotary¹⁰ motion of the Lagrangian particles that occurs when the acceleration and velocity vectors are not aligned with each other (e.g., motion induced by typical vortices). The second kinematic time describes the average rate of the deviations from the average rotary motion (e.g., when particles circulate inside a drifting vortex). In this paper, for simplicity, the idea of parametric randomization is illustrated with the Markov-2 model and the $T^{(1)}$, and extensions to other model parameters and to higher-order models are relatively straightforward.

The central idea of this paper is to consider $T^{(1)}$ as random parameter with prescribed statistical distribution—this step introduces a level of the *randomization* in the Markov model hierarchy. Instantaneous values of $T^{(1)}$ in the stochastic model correspond to the short-time averages in (4) and (5), used in (29). Each value of $T^{(1)}$ and the time-averaging interval, δt , imply a particular local kinematic event of the turbulence. In the randomized stochastic model, the distribution of $T^{(1)}$, $P^{(1)}[T^{(1)}; \mathbf{x}]$ (further, the superscript is often dropped for convenience), is implemented for a finite set of discrete values of $T^{(1)}$. For simplicity, and this assumption can be relaxed in the future, we consider only one population of particles in terms of their velocity variance, hence the N -value $P(T)$ implies that there are N distinct particle populations in terms of their acceleration variance. A random change of T implies that the particle experiences a transition from one population to another.¹¹ Physically, the transitions simulate migration of the particles between different types of the mesoscale currents.

The proper choice of δt is related to the physics of the problem. Obviously, in the limit $\delta t \rightarrow \infty$ a T dis-

¹⁰ In the absence of the stochastic forcing and in 2D, components of the first kinematic-time tensor are associated with motion of particles along the corresponding ellipses.

¹¹ The Markov-1 models with two populations of particles have been considered in the past (e.g., Luhar et al. 1996; Pasquero et al. 2001) but without transitions between the populations.

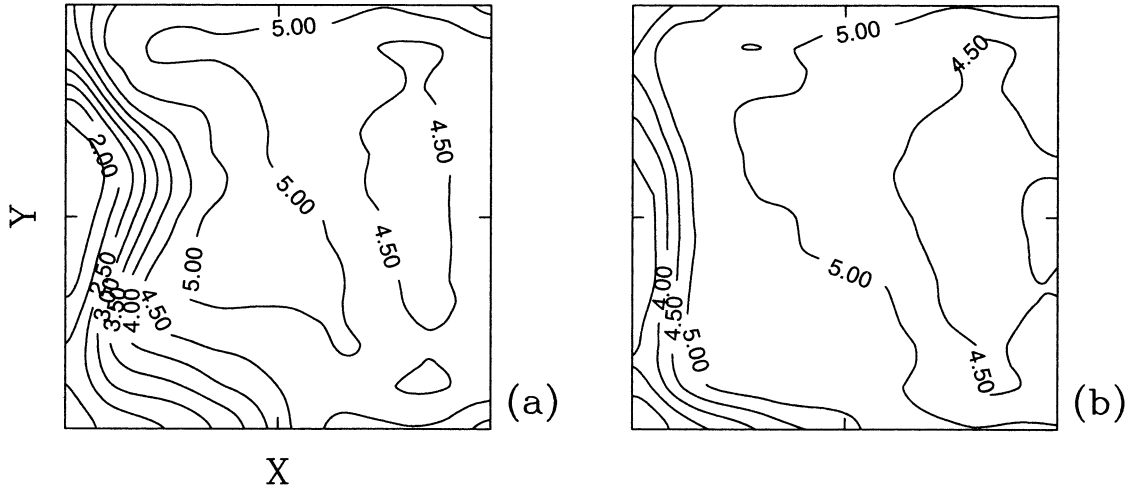


FIG. 2. Fluid-dynamic values of the average first kinematic time: $\langle M_1 \rangle = [M_1(P_x) + M_1(P_y)]/2$ in the (a) upper and (b) deep ocean (CI = 0.5 days).

tribution collapses to a δ function, and the equations reduce to the corresponding standard Markov model. In the numerical solutions of the oceanic gyres, the particles tend to move in a circular way or oscillate (although, with a big scatter in periods of oscillations), therefore an average period of oscillations is the natural physically justified choice of δt . Hence, we define the kinematic-event time interval locally as

$$\delta t = \pi T_\infty^{(1)}, \tag{32}$$

where $T_\infty^{(1)}$ is the first kinematic time obtained with the infinite-time averaging interval, as in BM. The δt is one half of the period associated with oscillatory Lagrangian motion induced by the coherent structures. It is easy to see that, if the Lagrangian particle motion is purely harmonic, that is $u \sim \sin(t/T + \phi)$, then (29) in combination with (32) yields the correct time scale:

$$\frac{\overline{u^2}}{\overline{\dot{u}^2}} = T^2 \frac{\int_0^{\pi T} \sin^2(t/T + \phi) dt}{\int_0^{\pi T} \cos^2(t/T + \phi) dt} = T^2. \tag{33}$$

Equation (32) could be improved by introducing the variable δt proportional to an instantaneous value of $T^{(1)}$, but this is not done here for the sake of simplicity. In the fluid-dynamic solution, δt is about 1–2 weeks and it is longer in the eastern and shorter in the western parts of the basin (according to Fig. 2).

In practice, the $P(T)$ is provided by either Eulerian or short-time Lagrangian (float) measurements of the turbulence; hence its estimate is, respectively, either exactly or approximately local in space. The normalization condition requires that

$$\int_{-\infty}^{+\infty} P(T) dT = 1, \tag{34}$$

and the distribution can be generally described by its statistical moments:

$$\begin{aligned} M_1(P) &= \int_{-\infty}^{+\infty} TP(T) dT, \\ M_2(P) &= \int_{-\infty}^{+\infty} [T - M_1(P)]^2 P(T) dT, \\ &\vdots \\ M_n(P) &= \int_{-\infty}^{+\infty} [T - M_1(P)]^n P(T) dT. \end{aligned} \tag{35}$$

For simplicity, we focus on the first four moments of $P(T)$ and their nondimensional characteristics: skewness.

$$\text{Sk}(P) = \frac{M_3(P)}{[M_2(P)]^{3/2}}, \tag{36}$$

and kurtosis,

$$\text{Ku}(P) = \frac{M_4(P)}{[M_2(P)]^2}. \tag{37}$$

In the gyres, the zonal, $P_x(T)$, and meridional, $P_y(T)$, components of $P(T)$ are found on a uniform 40×40 grid, in each layer, and for 100 uniformly distributed values of T . Each value of T is associated with distinct kinematic population of particles. In this paper we use the excessive resolution in T and, thus, avoid the corresponding sensitivity study; in practice, it is likely that a discretization level involving three to four distinct values of T would yield reasonably good solutions. The average values of $T^{(1)}$, $M_1(P)$, are rather isotropic and they are 4–5 days away from and 1–3 days inside the swift currents (Fig. 2). The $M_1(P)$ is typically larger in the zonal direction and in the upper ocean, and it is

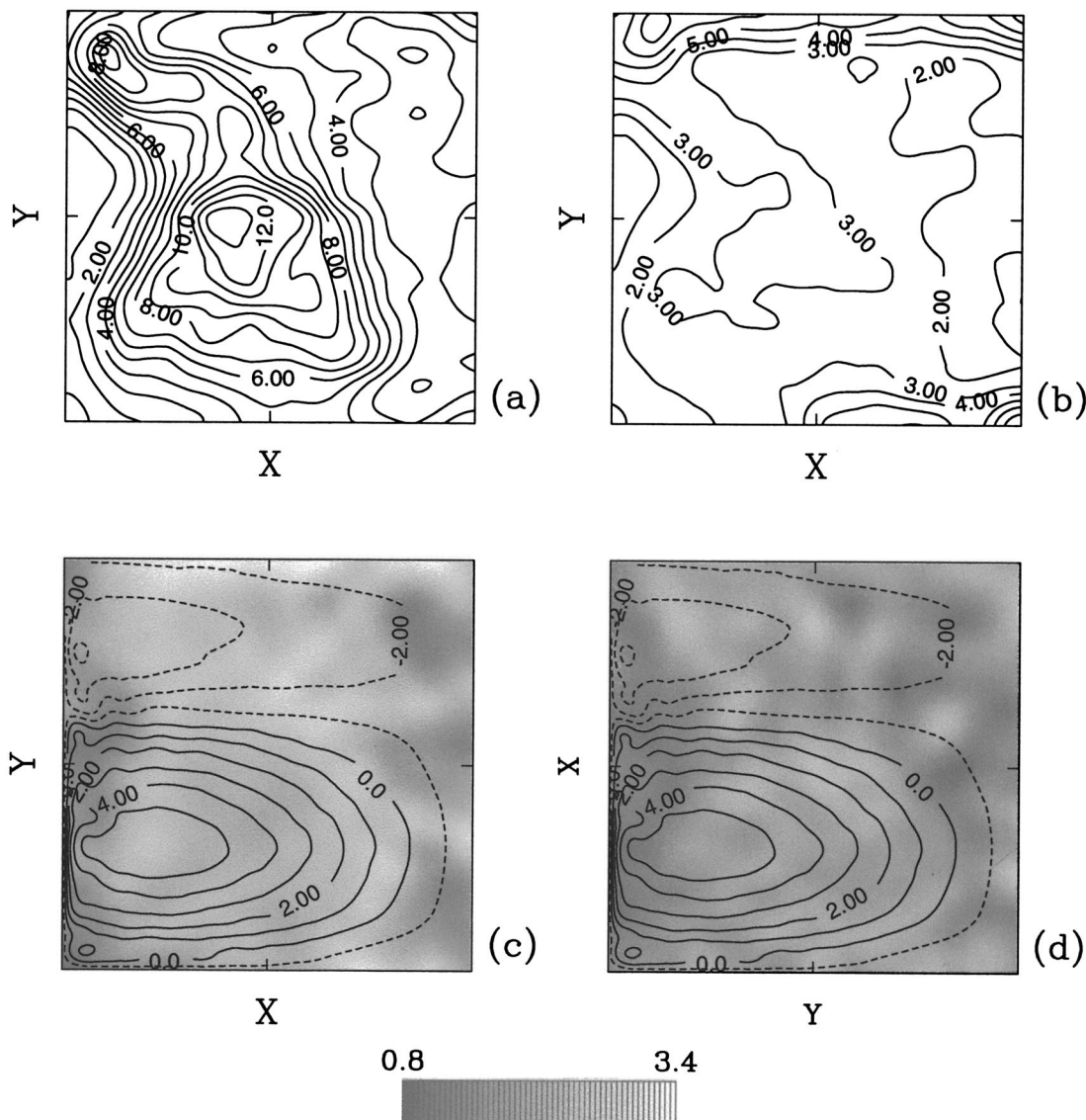


FIG. 3. Fluid-dynamic, upper-ocean (a) $M_2(P_x)$, (b) $M_2(P_y)$, (c) $Sk(P_x)$, and (d) $Sk(P_y)$ for the first kinematic time [(a), (b) $CI = 1 \text{ day}^2$; the upper-ocean velocity streamfunction is shown in (c), (d) with $CI = 0.25 \times 10^4 \text{ m}^2 \text{ s}^{-1}$].

smaller near and along the boundaries. The differences in the upper- and deep-ocean maps of $M_1(P)$ are noticeable but moderate (Fig. 2), and they roughly illustrate the level of differences in the other statistical moments (not shown for the deep ocean). The distribution of $M_2(P)$ is strongly anisotropic away from the WBCs (Figs. 3a,b), and $P_y(T)$ is more peaked than $P_x(T)$ (Figs. 4b,d); hence $M_2(P_y)$ is generally smaller. The regions of the fast (slow) spreading rates (i.e., the super- and subdiffusive behaviors) are characterized by the large (small) values of $M_2(P)$. That is shown with space averages of $P(T)$ over the central part of the basin characterized by $M_2[P_x(T)] > 10 \text{ day}^2$ (Fig. 4b), and over the eastern basin characterized by $M_2[P_y(T)] < 2 \text{ day}^2$ (Fig. 4d). In the WBCs $M_2(P)$ is almost isotropic—Fig.

4c shows $P(T)$ averaged over the area where each component of $M_2(P)$ is less than 2 day^2 . The basin-average $P(T)$ is dominated by contributions from the eastern basin, except for the small- T contribution from the WBCs (Fig. 4a). Thus, the broad (narrow) distributions are associated with fast (slow) spreading rates.

c. Eulerian velocity autocorrelation

The full Markov-2 model (12) simulates velocity statistics that can be treated only as the Lagrangian one. If the corresponding solution is obtained in the homogeneous mode with the local parameter values, that is, with parameters corresponding to the deployment location of particles, then we refer to it as the *local* Mar-

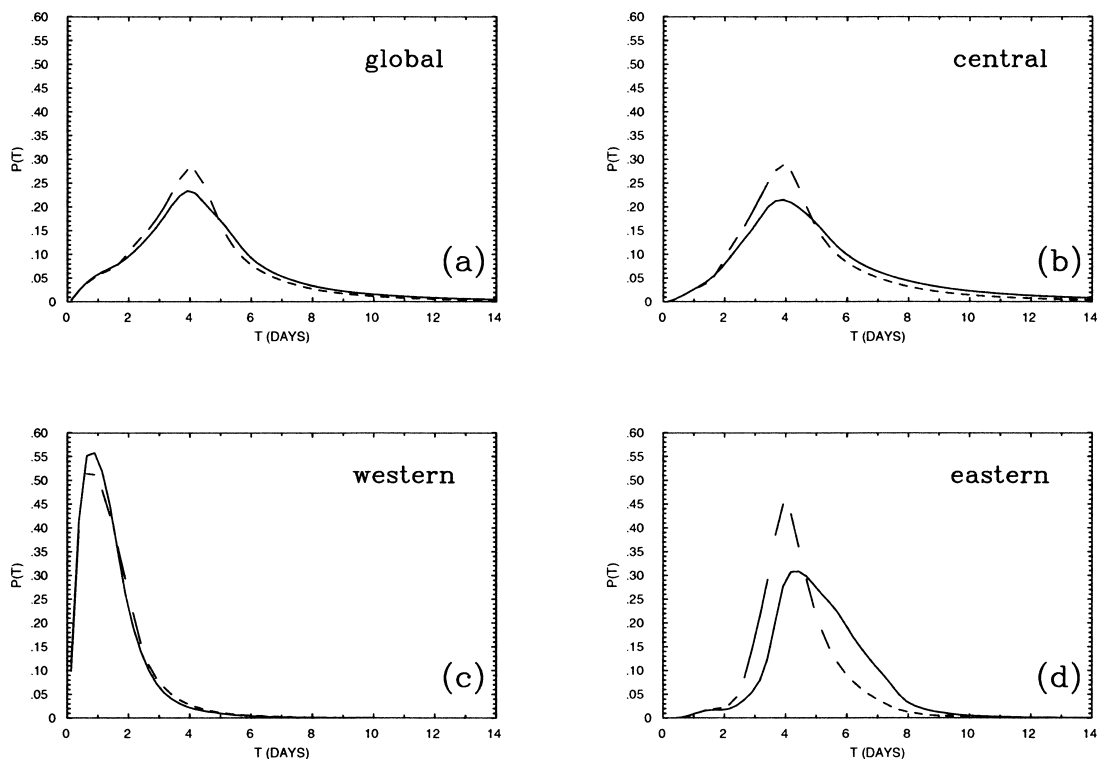


FIG. 4. The upper-ocean $P(T)$ averaged over the (a) basin area, (b) central region with large $M_2[P_x(T)]$, (c) WBCs, and (d) eastern region with small $M_2[P_y(T)]$. Solid and dashed lines correspond to the zonal and meridional components of the $P(T)$, respectively.

kov-2 solution. On the other hand, the reduced Markov-2 model without the first equation simulates exactly the same velocity statistics as the local model, but now the statistics can be treated as the Eulerian one. Hence, the fading-memory time parameter, θ , describes monotonic decay of the velocity autocorrelation function, which may be interpreted both as the Lagrangian and Eulerian quantity. This freedom of interpretation arises from the fact that the Markov models, so far, do not account for spatial correlations of the velocity field—if they would, then the reduced model solution could not be treated as the Eulerian one. The next important development along the research line followed in BMB, BM, and here, is to improve the models so that they locally account for both the temporal and spatial correlations (e.g., Kaneda et al. 1999), but this is beyond the scope of this paper.

The θ is the most difficult parameter to estimate because the monotonic decay is strongly overlapped by nonmonotonic, oscillating contributions to $R(\tau)$, induced by the coherent eddies. In BMB θ is estimated from the intermediate-time power laws fitted to $D'(t)$, but this algorithm is rather delicate and nonlocal. We propose to estimate θ locally, from monotonic decay of the envelope of the Eulerian velocity autocorrelation function, $R_E(\tau)$, defined in (16) with a velocity time series given at a fixed location rather than following a Lagrangian trajectory. Given often complicated and oscillating, fluid-dynamic $R_E(\tau)$ (Fig. 5), this algorithm is

not the final choice, but it is a first step toward understanding relations between $R_E(\tau)$ and the Lagrangian transport in turbulent fluids. This algorithm allows one to simulate the transport rather well (section 5).

Here $R_E(\tau)$ is calculated in each layer and in 40×40 uniformly distributed locations and with the whole time length of the fluid-dynamic solution. The intermediate-time qualitative features of $R_E(\tau)$ and $R(\tau)$ (BMB) are similar: strong oscillations and slow decay. (The latter quantity cannot be calculated for long-time intervals because it is nonlocal.) In the vicinity of the WBCs and their eastward jet extension, $R_E(\tau)$ is weakly oscillating with a shape close to exponential (Fig. 5a). There, the negative lobes of $R_E(\tau)$ are small in amplitude but robust in their occurrence. In the central part of the subtropical gyre, where the zonal spreading rates are enhanced and the values of $M_2(P_x)$ are large, the zonal component of $R_E(\tau)$ has enhanced positive lobes (Fig. 5b). Away from the swift currents, and more so in the eastern part of the basin, $R_E(\tau)$ exhibits strong oscillations and weak decay (Figs. 5c,d). The empirical envelope-decay laws are obtained by drawing the limiting curve, starting from the largest τ , that includes all maxima of $R_E(\tau)$. After some smoothing, the limiting curve represents the monotonically decaying envelope of $R_E(\tau)$. In principle, θ could be estimated from a functional fit (e.g., an exponential) to the envelope of R_E ; however, given the complexity of $R_E(\tau)$, θ is chosen

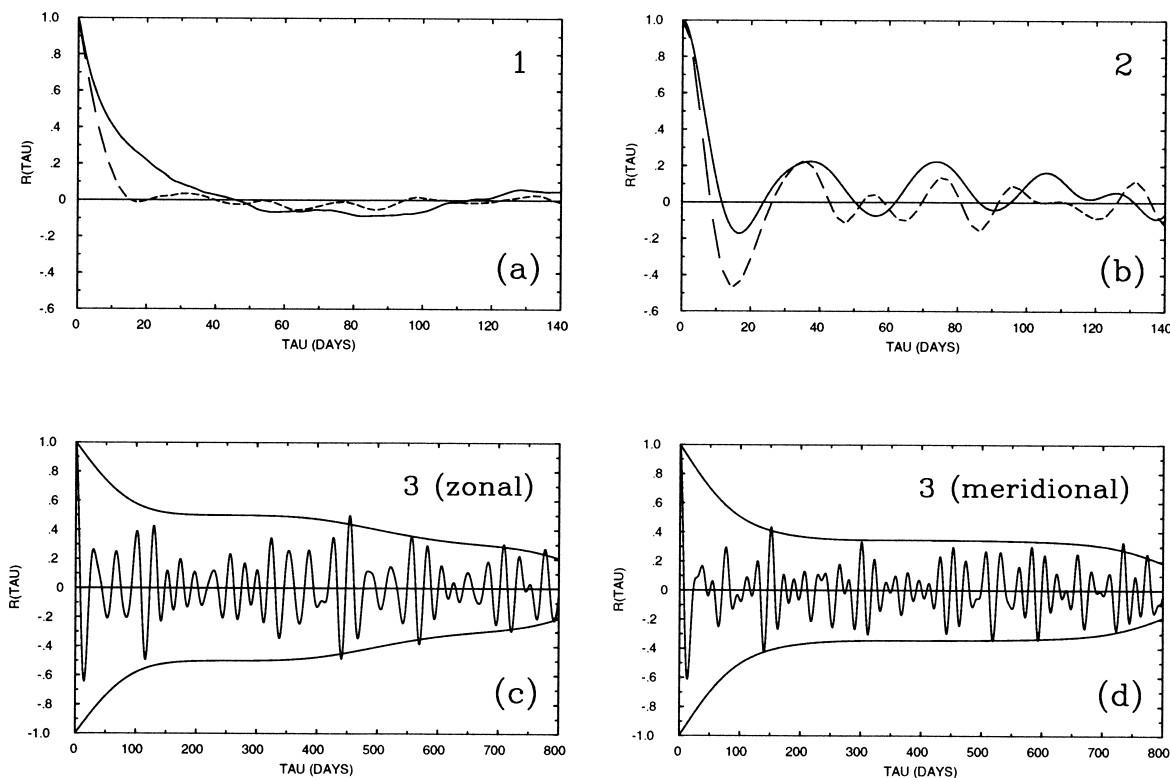


FIG. 5. Upper-ocean, Eulerian velocity autocorrelation functions, $R_E(\tau)$, in locations marked in Fig. 7. In locations (a) 1 and (b) 2, solid and dashed curves correspond to the zonal and meridional components of $R_E(\tau)$, respectively; the (c) zonal and (d) meridional components of $R_E(\tau)$ from location 3 are shown together with their smooth envelopes. The location number is specified on each panel.

more simply as the value of τ at which R_E equals some threshold, R_0 . We use $R_0 = 0.25$ because it is found empirically that this value yields the best results. The corresponding fading-memory time is shown in Fig. 6. Variations of R_0 by $\pm 30\%$ yield no qualitative changes of the transport, but the intergyre fluxes and local spreading rates vary by $\pm 15\%$, respectively. In the deep ocean, the values of θ are typically larger by 30% than

in the upper ocean, that is due to the slower decay rates of R_E .

4. Randomized Markov-2 model

This section studies the properties of a family of $T^{(1)}$ distributions with shapes qualitatively similar to those found in the gyres (section 3, Fig. 4) for

$$\begin{aligned}
 T > a: \quad P(T) &= \frac{(T-a)}{(b^2 + cd^2)} \left\{ \exp\left[-\frac{(T-a)}{b}\right] + c \exp\left[-\frac{(T-a)}{d}\right] \right\}, \quad d = mc, \\
 T < a: \quad P(T) &= 0.
 \end{aligned}
 \tag{38}$$

It is assumed that parameters a , b , and m are positive and c is nonnegative, and the normalization constant is given by (34). The (38) is a sum of two standard gamma distributions shifted by a (Karlin and Taylor 1975). The choice of (38) is convenient because the shape of P is qualitatively similar to the P shapes diagnosed from the gyre solutions and the low-order statistical moments of P are found analytically (appendix B). The parameters in the P distribution have only an academic interest—here they are introduced just to investigate the properties

of the new model. In practical applications, there is no need to fit these parameters because $P(T)$ has to be diagnosed from the turbulence without any parametric assumptions, as it is. Each distribution (38) has bell-like shape, with single maximum and slowly decaying tail at large T (Fig. 8c). For $0 < c < 0.1$ and $1 < m < 5$: Sk and Ku vary from 1.5 to 5, and from 3 to 50, respectively (Figs. 7a,b). These ranges and the relationship between Sk and Ku (Fig. 8d) are qualitatively similar to the fluid-dynamic properties (Fig. 8).

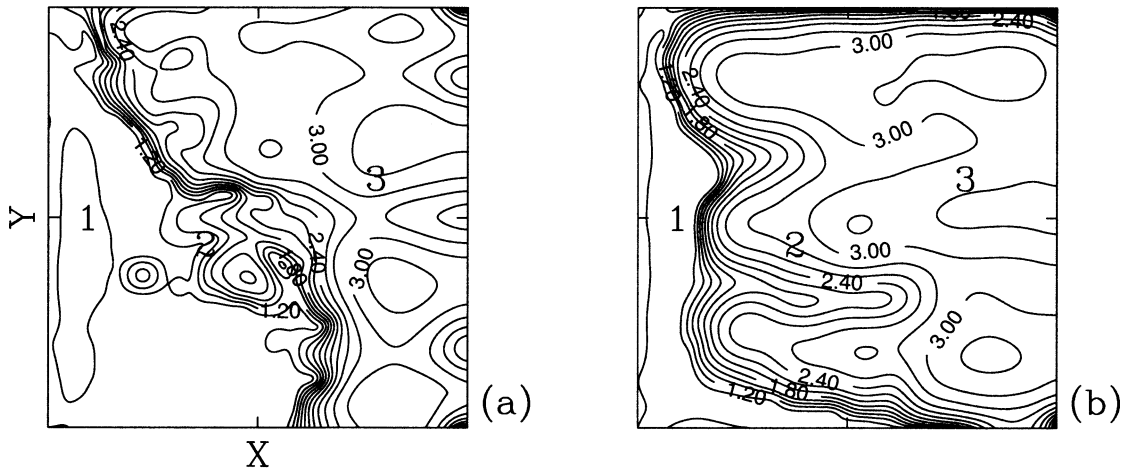


FIG. 6. The upper-ocean, fading-memory time, $\log_{10}\theta$, in the (a) latitudinal and (b) meridional directions (θ is in days; $CI = 0.2$). The digits 1, 2, and 3 mark locations used in Fig. 5.

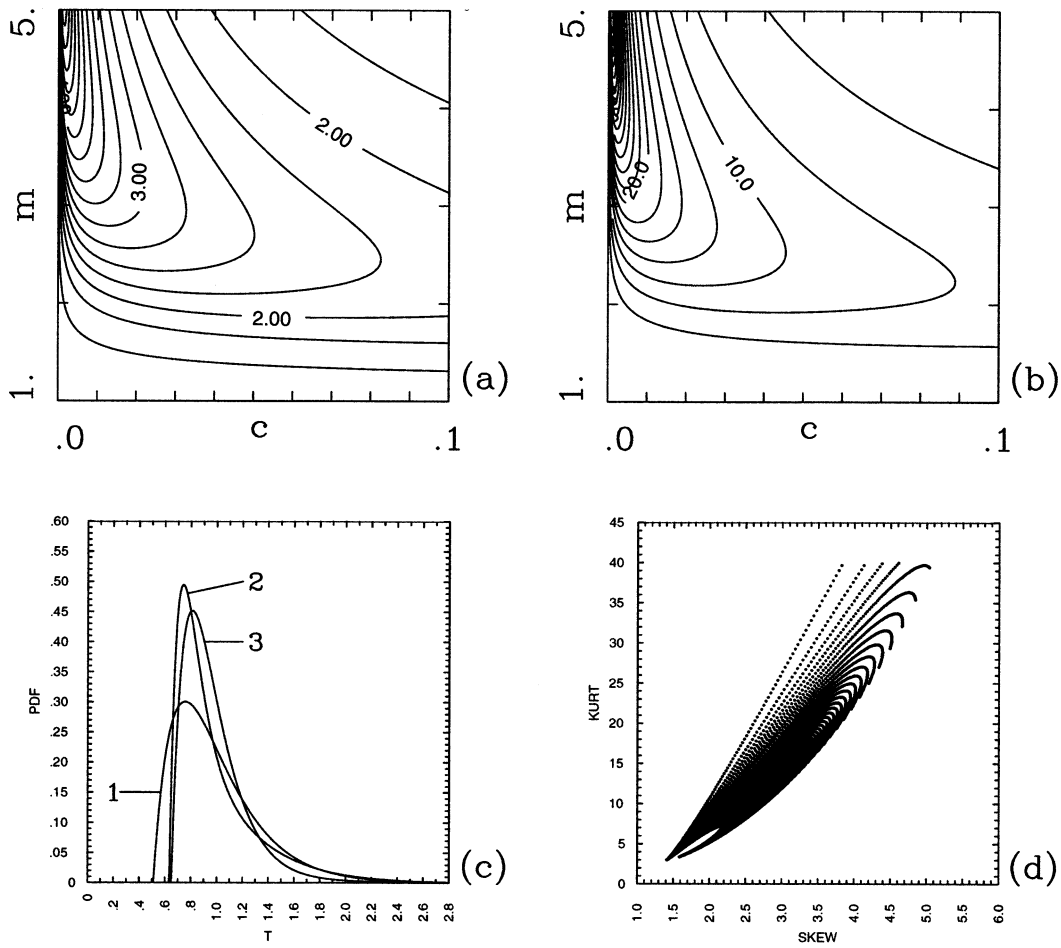


FIG. 7. (a) Skewness Sk and (b) kurtosis Ku of the analytical $T^{(\omega)}$ -distributions as the functions of c and m [see (38)] [(a) $CI = 0.25$, (b) $CI = 2.5$]. In (c) several different $P(T)$ are shown for 1) $c = 0, m = 1$, 2) $c = 0.1, m = 3$, and 3) $c = 0.015, m = 5$ (the curves are indicated by the corresponding numbers). (d) Scatterplot of the kurtosis shown in (b) vs the skewness shown in (a).

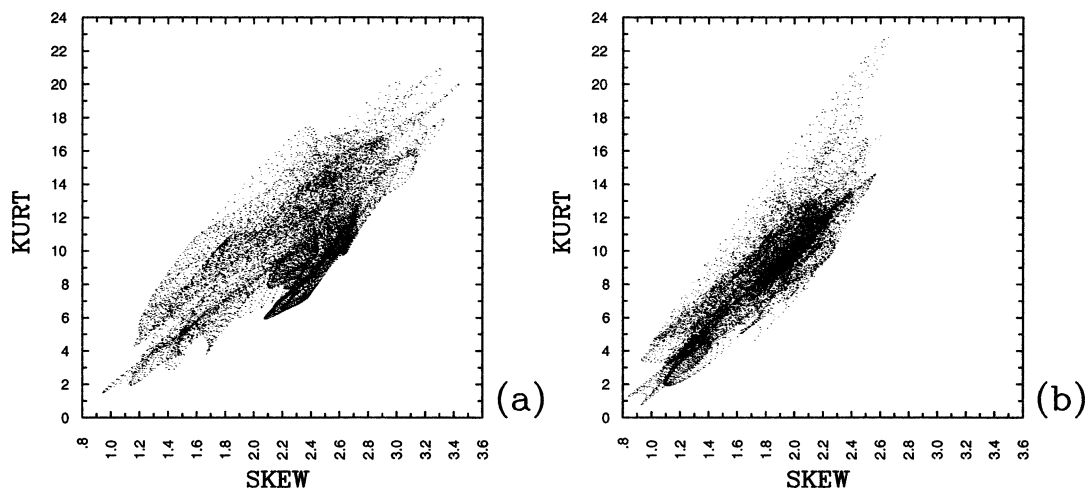


FIG. 8. Scatterplots of the fluid-dynamic, upper-ocean kurtosis vs skewness of $P(T)$ in the (a) zonal and (b) meridional directions. The samples are taken at uniformly distributed spatial locations.

Each value of $T^{(1)}$ from the distribution $P(T^{(1)})$ corresponds to certain population of particles, that is, to certain probability distribution of the Eulerian \mathbf{u}' and \mathbf{g} : $P_u(\mathbf{u}')$ and $P_g(\mathbf{g})$, respectively. The second moments of these distributions are connected by (29). For simplicity, it is assumed¹² that there is the single local value of σ_{ij} , and, therefore, the single local P_u for all values of $T^{(1)}$:

$$P_u(\mathbf{u}, \sigma) = (2\pi)^{-1} |\sigma|^{-1/2} \exp\left[-\frac{1}{2} u_i (\sigma^{-1})_{ij} u_j\right]. \quad (39)$$

In other words, the probability distribution of σ , $P_\sigma(\sigma)$, is the δ function. At each moment of time, the random forcing amplitude and $T^{(1)}$ of a stochastic particle, hence its acceleration, are characterized by an instantaneous value of ξ_{ij} . Here ξ_{ij} is statistically distributed according to its own distribution: $P_\xi(\xi)$. Given the probabilities of $T^{(1)}$ and σ , that is, $P[T^{(1)}]$ and P_σ , the probability to find each ξ_{ij} is uniquely determined by (29). For each value of ξ_{ij} , that is, for each population of particles, the probability to find a particular \mathbf{g} is

$$P_g(\mathbf{g}, \xi) = (2\pi)^{-1} |\xi|^{-1/2} \exp\left[-\frac{1}{2} g_i (\xi^{-1})_{ij} g_j\right]. \quad (40)$$

Particle transition from one value, ξ_M , to another value, ξ_N , that is, transition from one population to another, is described by the transition probability function:

$$P(g, \xi_M \rightarrow \xi_N) = C(\xi_M) \frac{P_g(g, \xi_N) P_\xi(\xi_M)}{P_g(g, \xi_M) P_\xi(\xi_N)}, \quad (41)$$

where the normalization factor,

¹² Relaxation of this assumption is straightforward, but adds some complexity.

$$C(\xi) = \int_0^\infty \left[\frac{P_g(g, \xi) P_\xi(\xi)}{P_g(g, s) P_\xi(s)} \right]^{-1} ds, \quad (42)$$

is such that the probability of all the possible transitions [including no transition, that is, $P(g, \xi_M \rightarrow \xi_N)$] is equal to unity. For example, if there are only two equally populated [i.e., $P_\xi(\xi_1) = P_\xi(\xi_2)$] populations: one characterized by smaller ξ_1 and the other by larger ξ_2 , then for large values of g_i : $P_g(g_i, \xi_2) \gg P_g(g_i, \xi_1)$ (40). Therefore, from (41) it follows that $P(g, \xi_1 \rightarrow \xi_2) \gg P(g, \xi_2 \rightarrow \xi_1)$; hence the particles with large g_i have enhanced probability to migrate from the small- ξ to the large- ξ population. The model is formulated so that transition from ξ_M to a nearby value, $\xi_M + \delta\xi$, can be less probable than transition to a distant value, ξ_N , however one can think of a physically grounded stochastic equation for ξ that would yield its continuous evolution—development of this idea is far beyond the scope of this paper.

Each population of particles has its own drift correction terms (10) and (13) characterized by its σ and ξ . Hence, the well-mixed condition is trivially satisfied for each population. The particle transitions between the populations preserve the well-mixed condition because they do not change (39), (40), and, therefore, given (41), they do not change the phase-space densities of the particle populations. In the inhomogeneous oceanic gyres, we verified the validity of the well-mixed condition by solving for the evolution of a large well-mixed population of particles.

The general properties of the randomization are found by calculating solutions of the isotropic, homogeneous, and stationary RM2 model, in an unbounded domain and for a sufficiently large number of particles. Here, $M_1(P)$ is chosen as the timescale [the corresponding $\beta^{(1)}$ is given by (30)], therefore its specific value is not important. The question is to what extent T_L and $D(t)$ de-

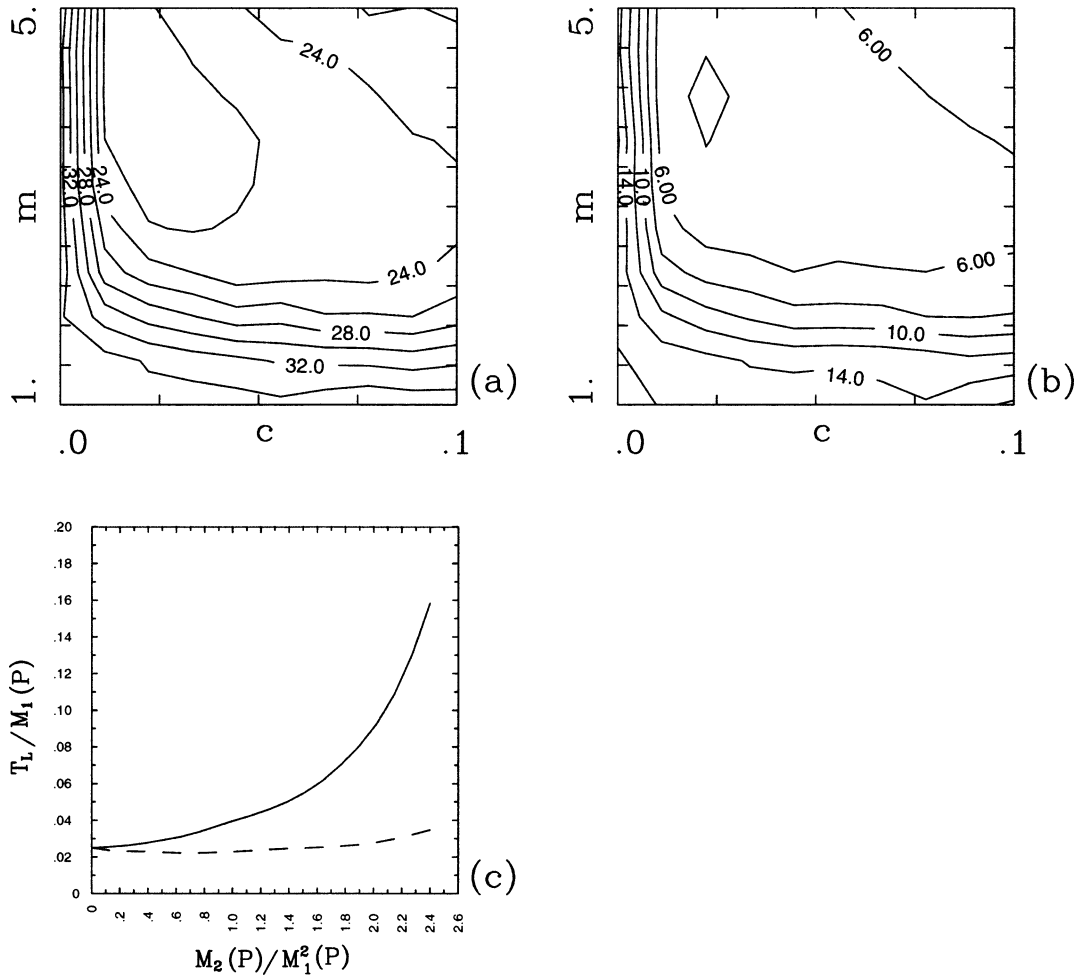


FIG. 9. Ratio $T_L/M_1(P)$ for (a) $\beta^{(1)} = 10$ and (b) $\beta^{(1)} = 100$, and for $M_2(P) = 2\sqrt{3}M_1^2(P)$ ($CI = 2 \times 10^{-2}$). (c) $T_L/M_1(P)$ as a function of $M_2(P)$ for $c = 0$ and $m = 1$; dashed and solid curves correspond to $\beta^{(1)} = 10$ and 100 , respectively.

pend on the P -distribution shapes. In the first experiment, c and m (hence, Sk and Ku) are varied as in Figs. 8a,b, and the second moment is kept fixed: $M_2(P) = 2\sqrt{3}M_1^2(P)$. It is found that large values of Sk and Ku correspond to smaller T_L and, therefore, to slower spreading rates in the large-time limit (Figs. 9a,b). Hence, when the distribution is more peaked, that is, Ku is large, the increased probability of small $T^{(1)}$, associated with slower spreading rates, dominates over unfrequent but large values of $T^{(1)}$ from the large- T tail of the distribution. If $\beta^{(1)} \rightarrow 0$, that is, $R(\tau)$ approaches an exponential, then T_L increases but the corresponding range of its variations decreases. In the second experiment, $M_2(P)$ is varied; Sk and Ku are kept fixed. It is found that the larger is $\beta^{(1)}$, the larger is variation of $T_L(M_2)$ (Fig. 9c). The difference due to the randomization is shown by comparing the RM-2 solution characterized by $P_{RM2}(T)$ at $c = 0$ and $m = 1$ (Fig. 7c) with the corresponding nonrandomized solution, that is, the one with $P_{M2}(T) = \delta[M_1(P_{RM2})]$. In the latter case, the

oscillations of $D(t)$ and $R(\tau)$ are larger in amplitude, and the spreading is generally slower (Fig. 10). Thus, the randomization damps oscillations of $R(\tau)$ (hence, broadens Lagrangian velocity spectrum) because it broadens the range of the simulated temporal behaviors. It has been shown previously (BM) that one of the main deficiencies of the nonrandomized Markov models is the excessively narrow range of simulated timescales—this paper offers a solution of this problem.

5. Application to oceanic gyres

a. Direct use of the RM-2 model

Two types of applications of the RM models are explored in this paper. The *direct* approach is to replace the traditional diffusion equation with an optimal RM model—in the given framework this is the most direct and accurate way to account for the presence of different populations of the coherent structures. The *interim* (in-

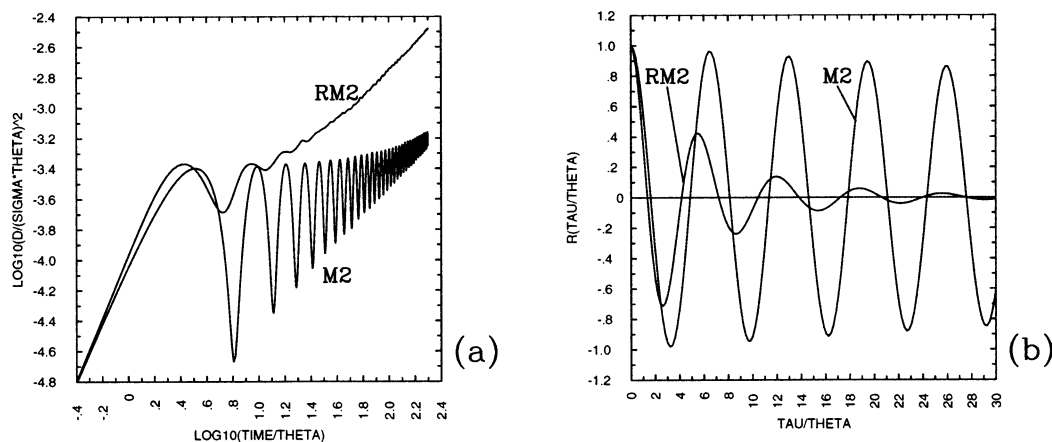


FIG. 10. (a) Single-particle dispersion, $D(t)$, and Lagrangian velocity autocorrelation function, $R(\tau)$, for $\beta_L^{(1)} = 100$, $c = 0$, and $m = 1$. The Markov-2 model is indicated by “M2,” and the RM-2 model with $M_2(P) = 2\sqrt{3}M_1^2(P)$ is indicated by “RM.”

direct) approach which is simpler but accounts for the effects of the coherent structures to a lesser degree, allows one analyze the ocean data with the RM formalism, to estimate the corresponding eddy diffusivity parameter, and then to simulate the transport with the corresponding diffusion model. In this section, both approaches are compared, and their systematic differences are identified.

In terms of the cross-gyre transport, the inhomogeneous RM-2 model performs quite well against the fluid-dynamic solution, both in the upper and deep ocean. However, there are discernible differences (Fig. 11) in the regions with enhanced spreading rates: in the central part of the subtropical gyre and along the lateral boundaries. It is expected that the RM-3 model, which simulates the intermediate-time superdiffusive spreading (BM), will compensate for the differences.¹³ The fluid-dynamic and RM-2 intergyre fluxes are qualitatively similar, except near the western boundary where the latter is much smaller (Fig. 12); therefore the total RM-2 fluxes are also slightly smaller than they should be (Tables 1 and 2). At first glance, this discrepancy is hard to explain because the approximate intermediate-time dispersion power law, $\alpha(x, y)$ shows no enhanced meridional spreading in this location (Fig. 1b). The explanation is that α is a fundamentally nonlocal property; therefore it can provide a distorted view on the spreading process in the presence of strong inhomogeneities.¹⁴ A detailed local analysis reveals that near the time-mean WBC separation point the meridional component of $R_L(\tau)$ has a very pronounced second positive lobe,

which is an indication of the superdiffusive spreading.¹⁵ It is expected that this behavior can be well simulated by an RM-3 model.

In contrast to the traditional estimates of T_L based on early truncation of $R(\tau)$ and nonlocal Lagrangian float information, the new randomized model is used to find T_L with locally estimated parameters, and the full, non-truncated $R(\tau)$. The zonal and meridional components of T_L (Fig. 13) are calculated by integrating locally estimated, that is, given by local homogeneous model, $R(\tau)$ in each layer and at 40×40 uniformly distributed grid points. The RM-2 parameters, $P(T)$, θ , σ , and ξ , are given by the fluid-dynamic solution, and the corresponding eddy diffusivity coefficient is found below. The largest values of T_L (about 8 days) are located in the zonally superdiffusive central part of the subtropical gyre, and the smallest values (less than 2 days) are in the subdiffusive eastern basin and some parts of the WBCs. The $T_L(x, y, z)$ pattern is somewhat similar to $\alpha(x, y, z)$ (Fig. 1), except along the boundaries. This is because the superdiffusive spreading is not represented in the second-order model, and for it one has to go one order higher in the hierarchy.

The eddy diffusivity, K_{RM2} , is found from (20) with the RM-2 T_L . It is strongly inhomogeneous and anisotropic, with the maximum values of about $30 \times 10^3 \text{ m}^2 \text{ s}^{-1}$ in the WBCs (Fig. 14). The diffusivity decreases with depth, and it is about 0.1 to $-0.5 (\times 10^3 \text{ m}^2 \text{ s}^{-1})$ in the eastern basin where the spreading rates are subdiffusive. Overall, the eddy diffusivity values are similar to the observed ones (e.g., Krauss and Böning 1987), except in the eastern basin where they are smaller.

¹³ Theoretically, a special $P(T)$ can exist that yields large and positive second lobe of $R(\tau)$, but this is not what we find in the gyres.

¹⁴ This statement is also true about the eddy diffusivity, which corresponds to $\alpha = 1$.

¹⁵ The Markov-3 model in BM does not pick up the enhanced near-boundary transport because it operates with nonlocally estimated parameters, and, therefore, it is not able to account for the relatively localized transport pathway.

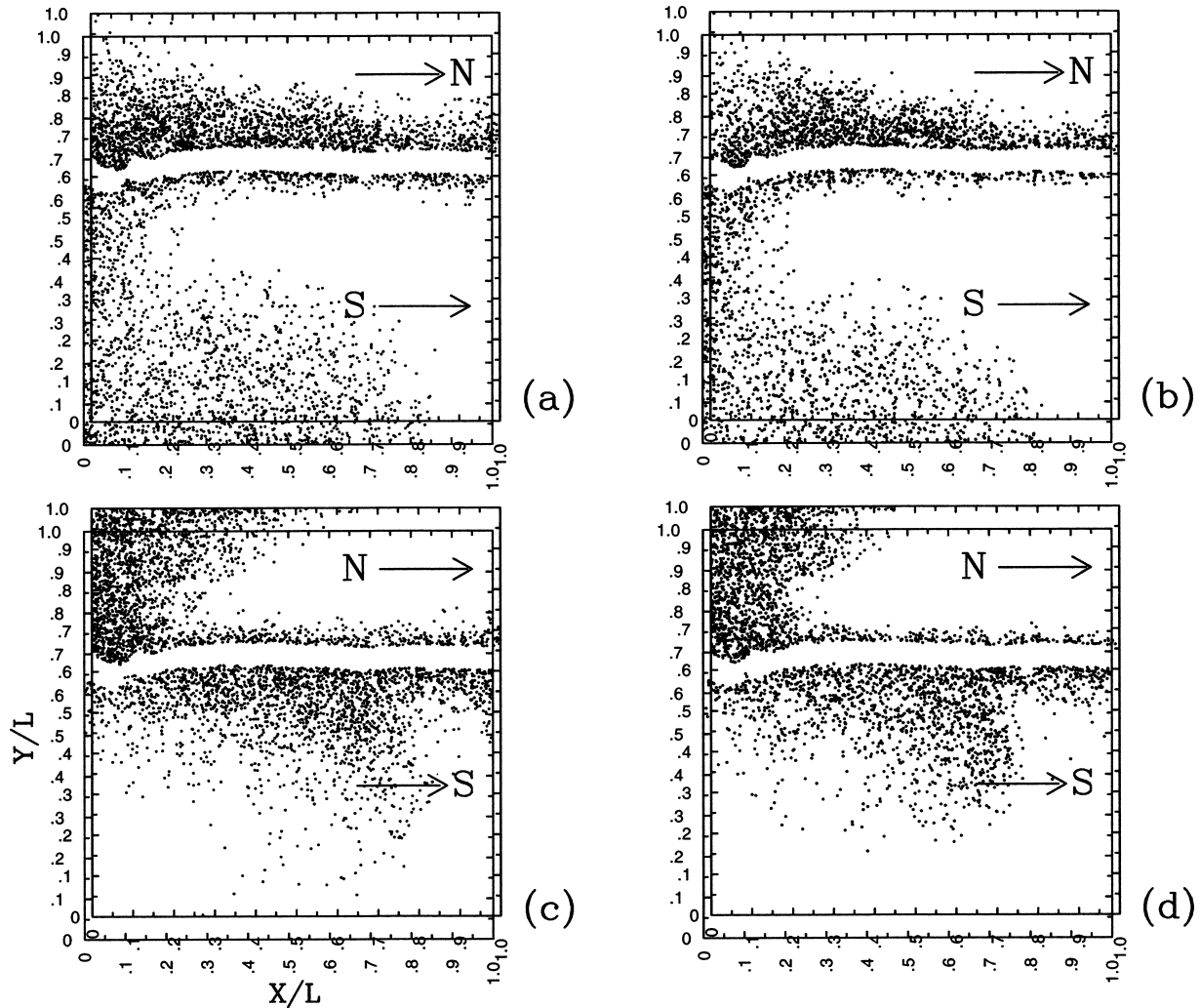


FIG. 11. Distributions of (a), (c) fluid-dynamic and (b), (d) RM-2 model, upper-ocean particles participating in (a), (b) northward and (c), (d) southward intergyre fluxes. Initial and final ($t = 500$ days) positions are shown on the same panels (slightly pulled apart, to indicate the gyres). The labels indicate which gyre (southern: S, or northern: N) the particles are leaving from (arrow to the right of the letter) or coming to (arrow to the left).

b. Comparison of the RM-2 and Markov-2 models

In general, the parametric randomization of a stochastic model significantly changes its transport properties (section 4). Here, the randomization consequences for simulating gyre-scale transport are addressed by comparing the intermediate-time evolution of particle distributions for both the RM-2 and the Markov-2 models as well as the fluid-dynamic model (Figs. 15 and 16). In the fluid-dynamic model, all the particle solutions are obtained by averaging over 5000 initial phases of the flow, which is substantially larger number than in BMB; hence the solution is found more accurately. We illustrate the randomization effect with a deployment location that is chosen away from the strong inhomogeneities. This is done in order to reduce their effect on the transport and in the subdiffusive part of the flow, where the second-order model is expected to perform

rather well; apart from this, the location and the corresponding transport properties are typical. The spreading process is quantified by calculating the rms length-scales of the particle distributions:

$$\Delta_i(t) = \sqrt{\langle [x_i(t) - \langle x_i(t) \rangle]^2 \rangle}, \quad (43)$$

where the angular brackets indicate a particle ensemble average, and the index corresponds to the coordinate direction. It is found everywhere in the basin that the randomization decreases the excessive oscillations of the Markov-2 $D(t)$ and $R(\tau)$, and it makes them more like the fluid-dynamic solution. This tendency is particularly pronounced in the subdiffusive parts of the basin where the oscillations are the largest, and the change of the transport properties due to the randomization is similar to the one shown in Fig. 10. In the particular example, this is expressed by improvements

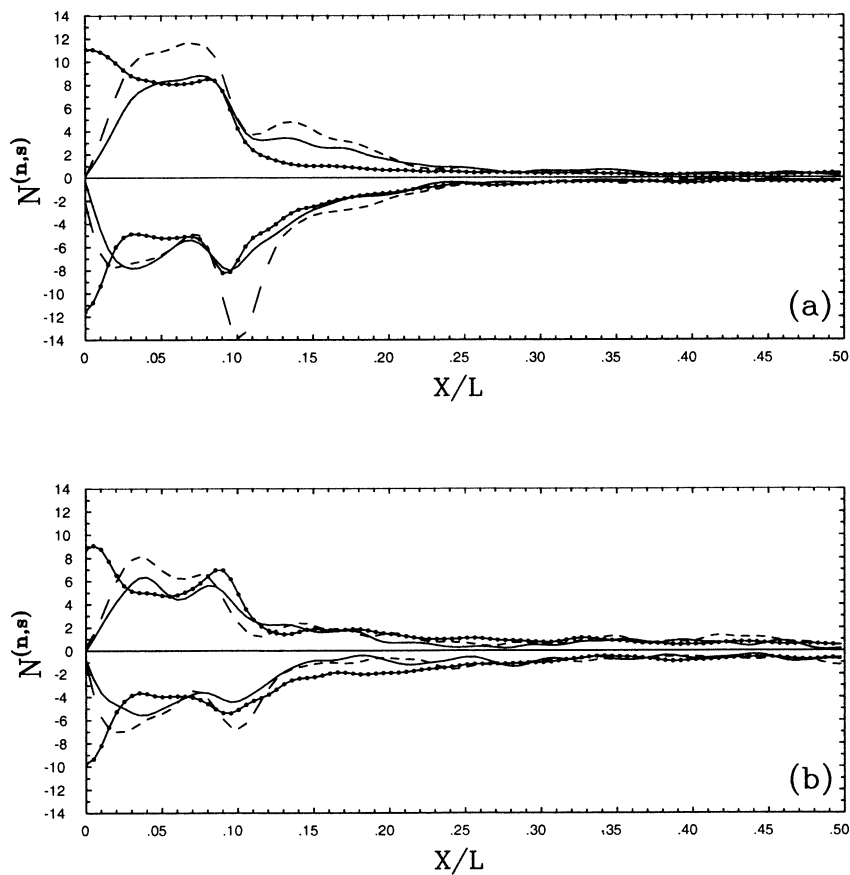


FIG. 12. The normalized, intergyre crossing distributions, $N^{(n,s)}(x)$, for $t = 500$ days and in the (a) upper and (b) deep ocean: the fluid-dynamic (dotted), RM-2 (solid), and M-0 (dashed curve) solutions. The positive and negative curves correspond to the northward and southward intergyre fluxes, respectively.

of $\Delta(t)$ shown in (Fig. 16). The excessive oscillations (as shown in BM) are the least attractive property of the standard stochastic model hierarchy. The spreading rate improvements due to the randomization go beyond damping the oscillations. Both the RM-2 and Markov-2 solutions underestimate the zonal component, $\Delta_1(t)$, by a factor of 2, although the RM-2 model performs systematically better (Fig. 16a). This is because the models are formulated as a second-order autoregressive processes for the velocities; therefore they are not capable of simulating the superdiffusive behavior (BM). The superdiffusive component of the zonal spreading is rather weak in this region (Fig. 1a); nevertheless its effect is seen by the enhanced migration of particles to the west (Fig. 15a). This behavior is consistent with the transport phenomenology reported in BMB and with the transport simulation improvement (see BM) obtained by going from the Markov-2 to -3 model, which captures the enhanced spreading rates. The meridional component, $\Delta_2(t)$, is much better simulated by the RM-2 than Markov-2 model; and the RM-2 solution is rather close to the fluid-dynamic one (Fig. 16b). This suggests that in the predominantly subdiffusive directions the com-

bin of the second order and randomization capture the essential physics of the transport by coherent eddies. Further transport improvements can be anticipated by fixing the shortcuts taken in this paper (see discussion in section 6).

The RM-2 and Markov-2 oceanic-gyre spreading rates are compared not only locally but also in the large-time diffusive limit. We find that the RM-2 eddy diffusivity, K_{RM2} , is generally larger than the Markov-2 one, K_{M2} , and the maximum difference is 2–4 times (Fig. 17). Consistently with the idealized studies (section 4), the largest difference between the two models is in the subdiffusive regions. The strong effect of the randomization is consistent with the idealized solutions in section 4.

c. Interim use of the RM-2 model

Here, the systematic differences are found between the transports simulated directly by the RM-2 model and indirectly by the advection–diffusion (Markov-0) model with K_{ij} estimated locally from the RM-2 model. The advection–diffusion (1) and M-0 models yield

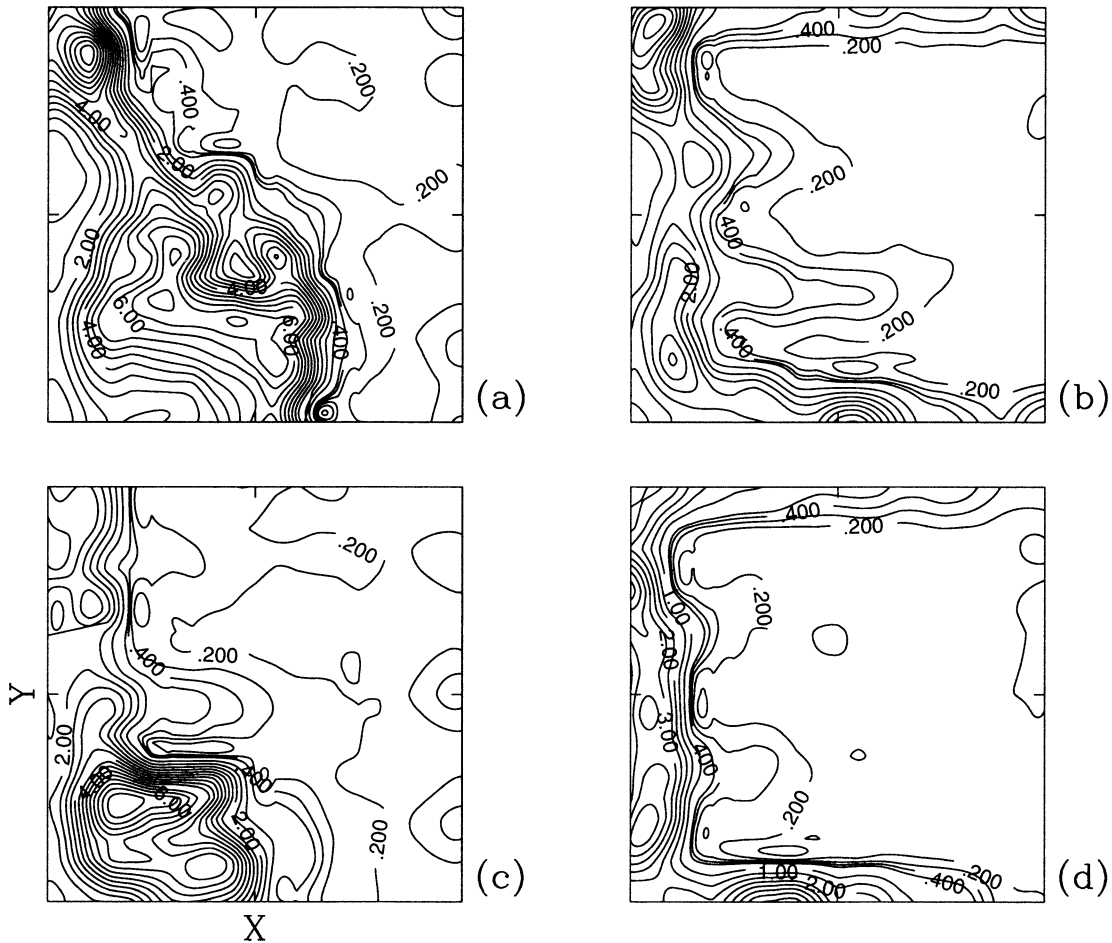


FIG. 13. (a), (c) Zonal and (b), (d) meridional T_z calculated in the (a), (b) upper and (c), (d) deep ocean with the RM-2 model and parameters locally estimated from the fluid-dynamic solution (CI = 0.5 days).

equivalent descriptions of the evolving tracer concentration, $c(t, \mathbf{x})$. However, the M-0 model is more general because it simulates not only $c(t, \mathbf{x})$, but also Lagrangian particle trajectories and material fluxes between any points of the domain. The inhomogeneous M-0 model is formulated in appendix C. It is found that the M-0 model, and, therefore, the whole indirect approach, substantially overestimates the average spreading rates and, therefore, the intergyre fluxes (Fig. 12, Tables 1 and 2). The overestimate is 20%–25% at later times, and it is somewhat larger in the upper ocean.

The systematic overestimate of the spreading rates can be explained as follows. The correction in $D(t)$ to the diffusive regime is represented by the second rhs term in (19). For the following, (22) is used and the two generic situations are considered:

$$\beta^{(1)} \gg 1: \quad \frac{2\pi}{T^{(1)}} \gg \frac{1}{\theta}, \quad (44)$$

which is common in the eastern, subdiffusive part of the basin and in the deep ocean; and

$$\beta^{(1)} \leq 1: \quad \frac{2\pi}{T^{(1)}} \leq \frac{1}{\theta}, \quad (45)$$

which is common in the swift currents and in the upper ocean. For the following, we introduce

$$\cos\phi = \theta^{-1} \{ \theta^{-2} + (2\pi)^2 [T^{(1)}]^{-2} \}^{-1/2}. \quad (46)$$

In the case of (44) $F \rightarrow \pi/2$; hence the large-time correction to the asymptotic diffusive regime is

$$\begin{aligned} D_{\text{CORR}} &= -2\sigma \int_0^\infty \tau R(\tau) d\tau \\ &= -2\sigma \frac{\sin(F + 2\phi)}{\sin(F) \{ \theta^{-2} + (2\pi)^2 [T^{(1)}]^{-2} \}} \\ &\approx 2\sigma \frac{1 - 2 \cos^2\phi}{\{ \theta^{-2} + (2\pi)^2 [T^{(1)}]^{-2} \}} \approx \frac{2\sigma [T^{(1)}]^2}{(2\pi)^2} > 0. \end{aligned} \quad (47)$$

This correction is positive, which implies that the Markov-0 model underestimates the corresponding Markov-

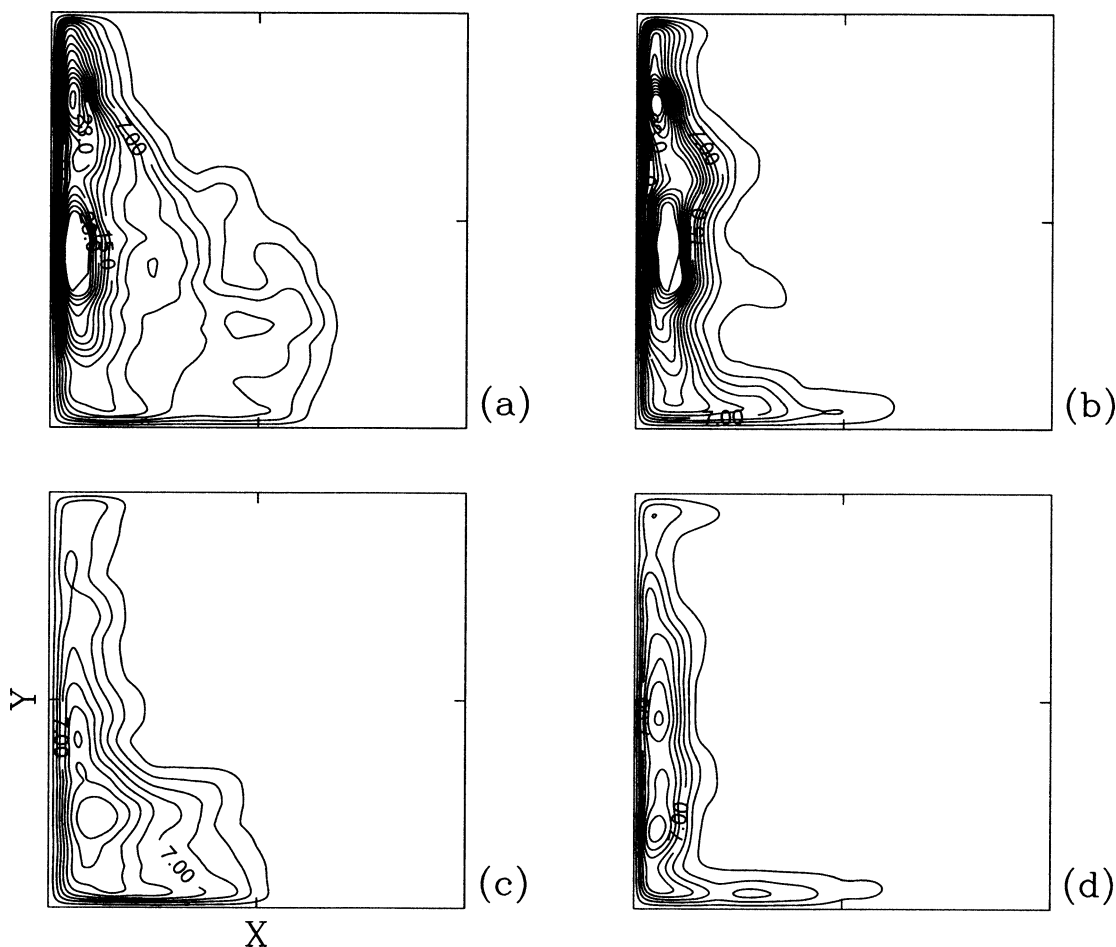


FIG. 14. The (a), (b) upper- and (c), (d) deep-ocean eddy diffusivity coefficients estimated with the RM-2 model: (a), (c) zonal and (b), (d) meridional directions ($CI = 2 \times 10^3 \text{ m}^2 \text{ s}^{-1}$).

$2D(t)$ (Fig. 18a). In the case of (45) $F \sim 2\pi\theta/T^{(1)}$, and, by using $\sin(F) \sim F$, $\cos(F) \sim 1$, and the second rhs expression from (47), one finds that

$$D_{\text{CORR}} \approx -2\sigma \frac{\{3\theta^{-2} - (2\pi)[T^{(1)}]^{-2}\}}{\{\theta^{-2} + (2\pi)^2[T^{(1)}]^{-2}\}^2} \quad (48)$$

$$\approx -6\sigma\theta^2 < 0.$$

This correction is negative; hence $D(t)$ is overestimated by the Markov-0 approximation to the Markov-2 model (Fig. 18b). In the fluid-dynamic solution, most of the upper-ocean intergyre flux occurs in the western basin, where $\beta^{(1)}$ is relatively small (as in Fig. 18a), and in the eastern basin, where $\beta^{(1)}$ is large (as in Fig. 18b), the flux is small. This explains the systematic overestimates by the Markov-0 approximation.

d. Alternative approaches to estimating T_L

The key component of the eddy diffusivity coefficient (20) is T_L . Traditionally, T_L is estimated directly from

the observed float $R(\tau)$ and the truncated approximation of (17):

$$T_L^* = \int_0^{\tau^*} R(\tau) d\tau, \quad (49)$$

and the key assumption is that $R(\tau)$ decay to zero fairly rapidly (e.g., Freeland et al. 1975; Colin de Verdiere 1983; Krauss and Böning 1987). This approach is fundamentally nonlocal; therefore, at least for partial locality one is tempted to use shorter float trajectories. At the same time, $T_L^* \rightarrow T_L$ when $\tau^* \rightarrow \infty$, and this suggests using longer trajectories. For statistically reliable calculation of $R(\tau)$, the time interval of trajectories has to be substantially longer than τ^* . This apparent contradiction has not been solved on the fundamental level, but in practice its consequences are minimized by choosing some compromise, intermediate value of τ^* .

In this paper, the estimates of T_L are local and exact in the formal sense. The estimates involve 1) extracting the local kinematic information from the observed float

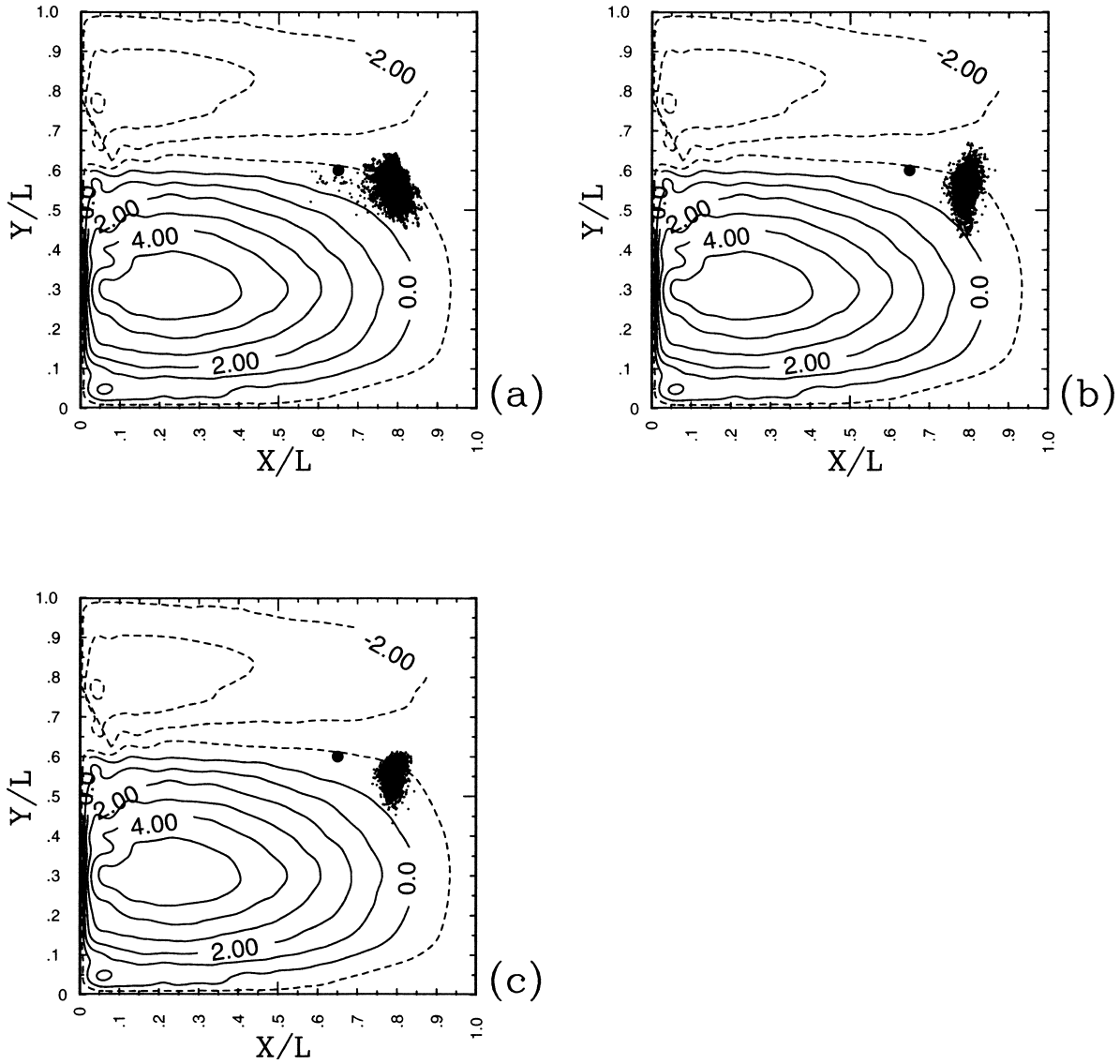


FIG. 15. Upper-ocean distributions of particles as given by the (a) fluid-dynamic, (b) RM-2, and (c) Markov-2 models, 250 days after the deployment. The particle distribution in (c) corresponds to the locally average value of Δ_2 over the oscillation period (cf. Fig. 16b); the corresponding Δ_1 is close to its local maximum (cf. Fig. 16a). Initial location of the particles is indicated by the filled circle. The time-mean velocity streamfunction is shown with $CI = 10^4 \text{ m}^2 \text{ s}^{-1}$.

trajectories (or, equivalently, from the Eulerian observations), 2) using this information to obtain the stochastic model parameters, 3) calculating $R(\tau)$ from the local homogeneous stochastic model, and 4) using this information and (17) to find T_L . Here, T_L found locally with the RM2 model is compared with T_L^* calculated directly from the Lagrangian particle trajectories, and for commonly used values of τ^* .

Small values of τ^* (≈ 10 days) yield $T_L^* \approx T_L$ in the WBCs, where $R(\tau)$ is relatively close to the exponential with fast-decay scale (BMB), but they yield very large errors in the eastern part of the basin where $R(\tau)$ oscillates stronger. With more practical $\tau^* = 50$ days,

$T_L^*(x, y)$ varies from 2 to 10 days (Figs. 19a,b), and it qualitatively¹⁶ captures the distribution of the sub- and superdiffusive regions. However, quantitatively $T_L^*(x, y)$ is very different from T_L in the eastern part of the basin where oscillations of $R(\tau)$ decay slowly (Figs. 19c,d). This suggests that one has to be very cautious in interpreting T_L^* as T_L . In particular, the difference between these quantities can explain poor predictions of the observed large-time spreading rates (e.g., Fig. 10 in Krauss

¹⁶ Although $T_L^*(x, y)$ may look reasonable, a stochastic model based on it strongly overestimates the spreading rates, as shown in BM.

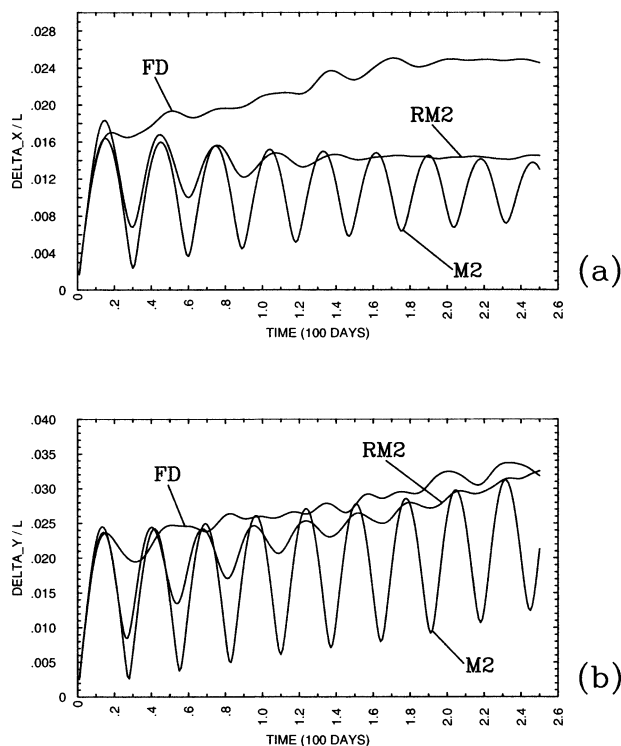


FIG. 16. The (a) $\Delta_1(t)$ and (b) $\Delta_2(t)$ corresponding to the particle distributions in Fig. 15. The labels FD, RM2, and M2 indicate the fluid-dynamic, RM-2, and Markov-2 solutions, respectively.

and Böning 1987; zonal spreading in Lumpkin and Flament 2001).

The assumption that T_L is determined by the curvature of $R(\tau)$ at $\tau \rightarrow 0$ leads to the conclusion (Babiano et al. 1987) that T_L is simply related to the local entrophy density, Z :

$$T_L = (2\pi/3)^{1/2} Z^{-1/2}, \quad Z = \overline{|\nabla \times \mathbf{u}|^2}/2. \quad (50)$$

The direct test of (50) is straightforward: the value of $Z^{1/2}$ is plotted against the corresponding value of T_L at each grid point (Fig. 20a). As a result of that, the relationship (50) is not confirmed, and no simple functional dependence of T_L on the small- τ curvature of $R(\tau)$ is found. The eastern part of the basin yields very small values of $Z^{1/2}$ with the full range of T_L values, and (50) is not even close to approximating their relationship. This is because the intermediate- and large- τ properties of $R(\tau)$ (hence, T_L) strongly vary across the flow, but its small- τ behavior does not. In the western basin, larger values of $Z^{1/2}$ generally correspond to smaller values of T_L , that is, the same tendency as in (50); however, most of the corresponding points in Fig. 20a are located below the line defined by (50).

Stammer (1998) proposed that T_L can be simply related to the time-mean vertical shear and stratification.¹⁷

¹⁷ A similar theory that accounts also for the horizontal stratification is in Visbeck et al. (1997).

$$T_L \sim \frac{\sqrt{\text{Ri}}}{f}, \quad \text{Ri} = \frac{N^2}{W},$$

$$W = \overline{\left(\frac{\partial u}{\partial z}\right)^2 + \left(\frac{\partial v}{\partial z}\right)^2}, \quad (51)$$

where Ri is called the mean Richardson number, f is the Coriolis parameter, and N^2 is the mean buoyancy frequency. The main physical assumption behind this scaling is that the major eddy source in the ocean is local baroclinic instability. Although this assumption can be generally correct, this paper demonstrates that a lot of information that has direct and large influence on T_L , in particular, and on the spreading process, in general, is hidden in kinematic details of the turbulence, as they are given by different populations of the coherent structures. This information is not present in simple scaling laws. In the fluid-dynamic model, and in the upper ocean (51) can be tested by using $du/dz \sim u_1 - u_2$ and by plotting $W^{1/2}$ versus T_L^{-1} . In the western basin, where the eddies are generated mostly by the baroclinic instability (e.g., Berloff and McWilliams 1999a,b), there is an approximate linear relationship between $W^{1/2}$ and T_L^{-1} (the upper group of points in Fig. 20b, with $W^{1/2} > 10 \text{ cm s}^{-1}$), as implied by (51). In the eastern basin dominated by the planetary waves, the dynamics is different; hence (51) does not hold even approximately (the lower group of points). Although (51) can, possibly, capture the essential basic physics, it cannot provide the corresponding nonuniversal proportionality coefficient, unlike the stochastic model formalism.

e. Search for a parameter closure

Full parameterization of the oceanic transport by mesoscale eddies requires a closure that relates parameters of a transport model to properties of the time-mean flow. The search for such closure and understanding of the physics behind it requires intensive studies far beyond the modest goals of this paper; however, an immediate and simple question is: to what extent the RM-2 model parameters, that is, the turbulence properties, are related to the time-mean velocities and their gradients? One idea, used in atmospheric and oceanographic modeling (Smagorinsky 1993), is similar to the mixing length theory of turbulence, and it yields the following relationship for the eddy diffusivity:

$$K \sim S \equiv \sqrt{s_{11}^2 + s_{12}^2 + s_{21}^2 + s_{22}^2},$$

$$s_{ij} = \frac{1}{2} \left(\frac{\partial \bar{u}_i}{\partial x_j} + \frac{\partial \bar{u}_j}{\partial x_i} \right). \quad (52)$$

The hypothesis (52) is tested by plotting $\sqrt{|K_{ij}(x, y)|}$, obtained in section 5a, versus $S(x, y)$ for an array of sample points, which uniformly cover the whole basin (Fig. 21). The scatterplot shows that (52) is largely irrelevant for the upper-ocean oceanic gyre turbulence, and this is also true in the deep ocean (not

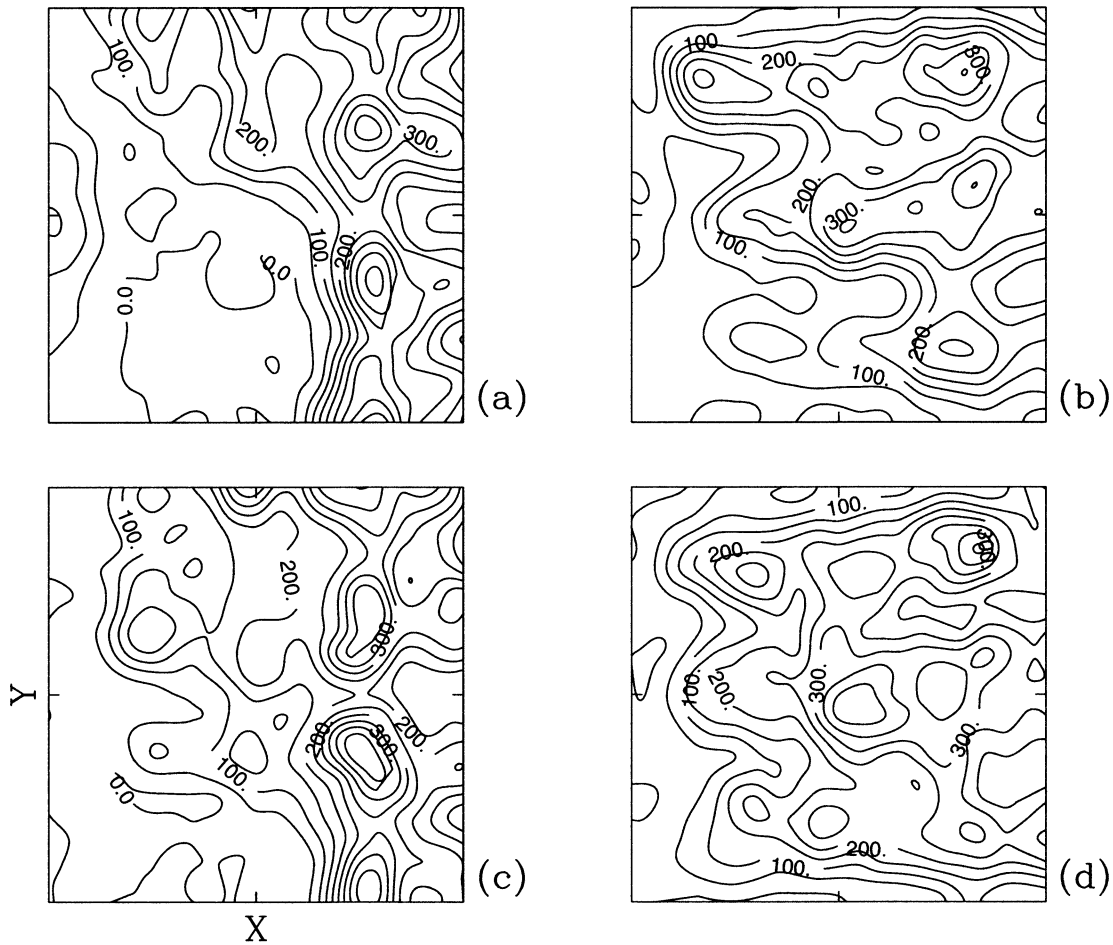


FIG. 17. The (a), (b) upper- and (c), (d) deep-ocean RM-2 correction, $E = (K_{RM2} - K_{M2})/K_{M2}$, to the Markov-2 eddy diffusivity coefficient in the (a), (c) zonal and (b), (d) meridional directions (CI = 50%).

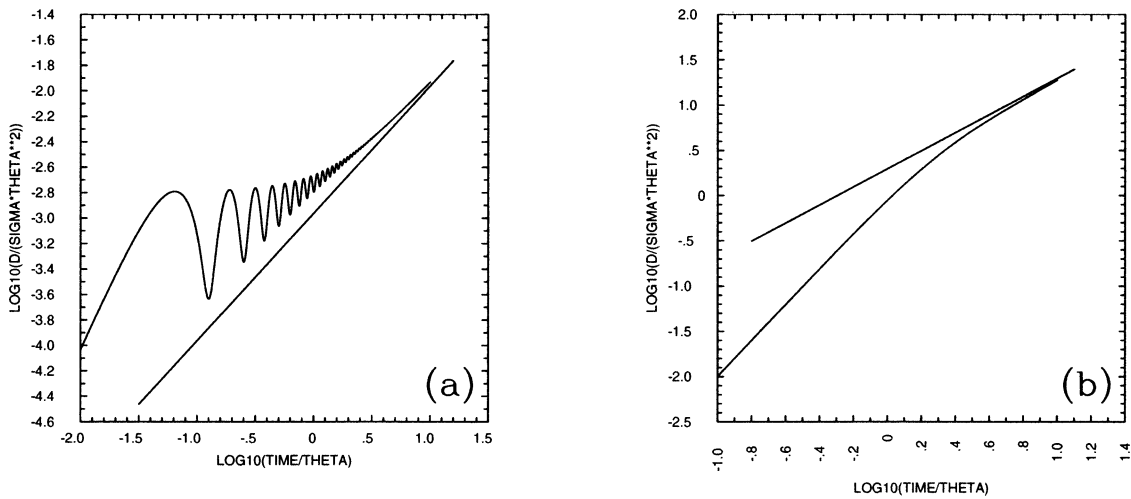


FIG. 18. The Markov-2 $D(t)$ in the regimes with (a) $\beta^{(1)} = 50$, and (b) $\beta^{(1)} = 1$. The straight lines indicate the large-time asymptotic diffusive behaviors.

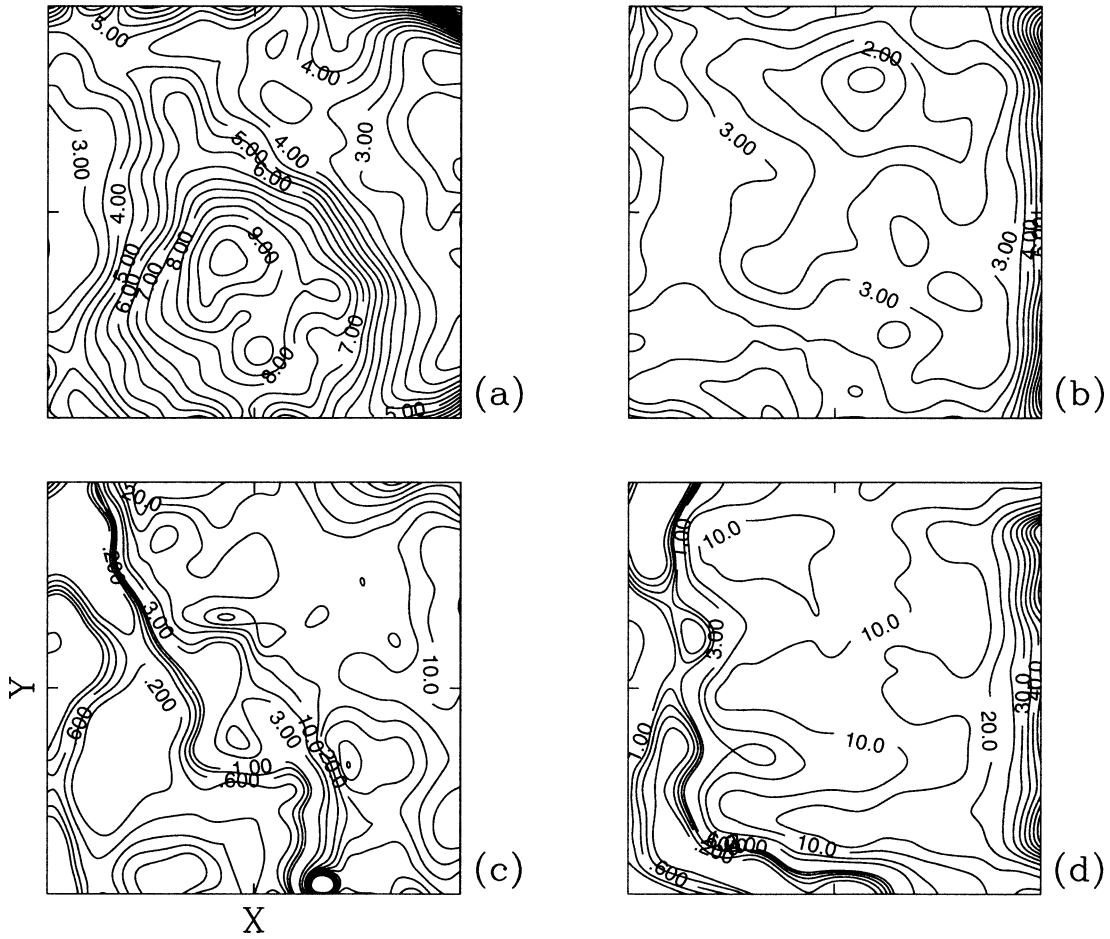


FIG. 19. The upper-ocean (a) zonal and (b) meridional components of T_L^* (CI = 0.5 days), and the corresponding errors, $E = (T_L^* - T_L)/T_L$, in the (c) zonal and (d) meridional directions (CI = 0.2 for $E \leq 1$, contour $E = 3$ is shown separately, and CI = 5 otherwise).

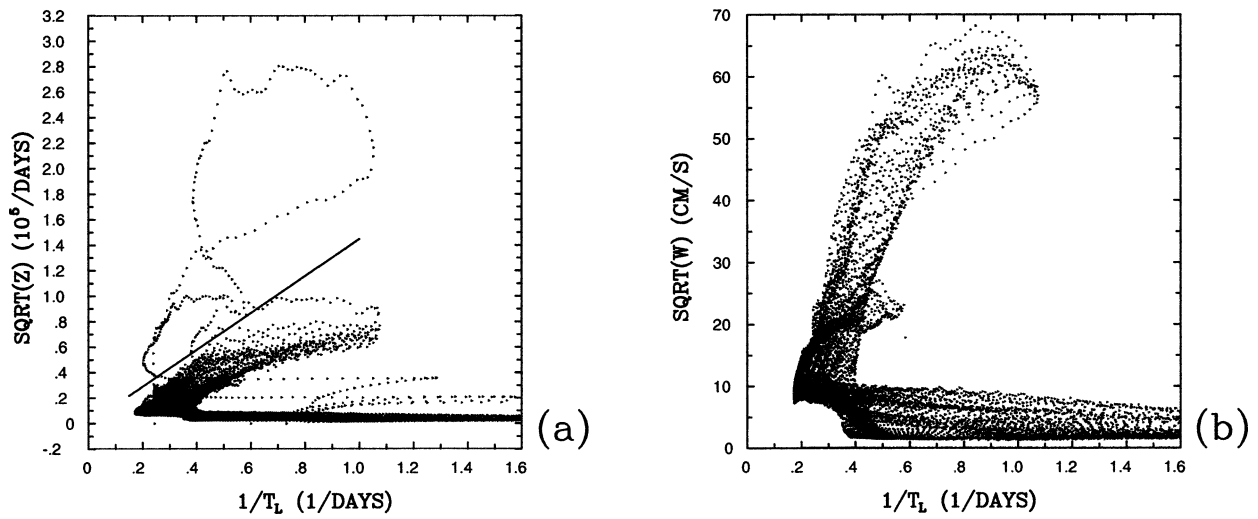


FIG. 20. Scatterplots of the upper-ocean (a) $Z^{1/2}$ and (b) $W^{1/2}$ vs T_L^{-1} . The straight line in (a) indicates (50).

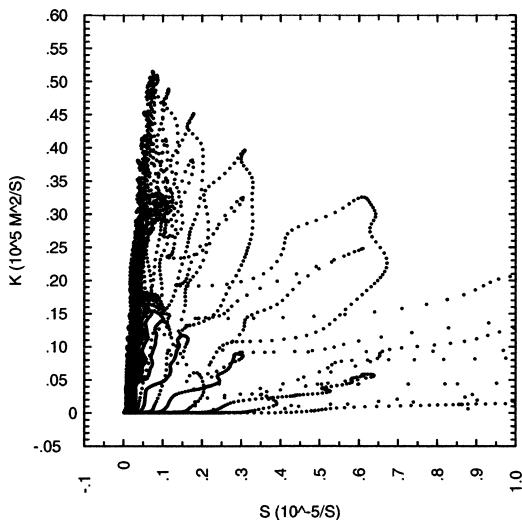


FIG. 21. Scatterplots of the upper-ocean $\sqrt{|K_{ij}|}$ vs S .

shown). Other simple closure hypotheses for such well-defined transport parameters as σ and $T^{(1)}$ also have been tested. The hypotheses are based on the dimensional arguments and they imply the following relationships: $\sigma \sim \bar{u}^2$ (eddy kinetic energy is proportional to the time-mean flow energy); $1/T^{(1)} \sim d\bar{u}/dz$; $1/T^{(1)} \sim d\bar{u}/dx$. For brevity, the corresponding scatterplots are not shown here, but in terms of the large scatter they are all qualitatively similar to (Fig. 21). Overall, the scatterplots yield little support to these simple closure hypotheses. Several reasons can be suggested for this. First, unlike the stochastic transport model, the time-mean velocity contains virtually no information on the structure and correlations of the eddy field, which are crucial for the transport. Second, the dynamical mechanisms supporting the eddies are substantially inhomogeneous and non-local—for example, the rings generated by the WBC eastward jet extension travel far away from the jet; the planetary wave population in the eastern part of the basin (Jiang et al. 1995; Berloff and McWilliams 1999a) is driven by instabilities in the western part of the basin—therefore, at a given location the transport parameters are poorly related to the time-mean velocity and its derivatives.

6. Conclusions and discussion

Our general goal is to look for turbulent transport models that account for the broadest variety of different Lagrangian motions in oceanic mesoscale turbulence. The main hope is that such models can be implemented in coarse-grid general circulation models as skillful parameterizations of the transport induced by unresolved eddies; they are potential replacements for the less skillful but commonly used diffusion model. The more specific goal of this paper is to advance the standard hierarchy of stochastic transport models, high-order mem-

bers of which are capable of simulating turbulent transport in the presence of nontrivial temporal correlations induced by coherent fluid structures. In these models, the passive tracer transport is represented by random motion of Lagrangian particles, and the tracer concentration is obtained by simple coarse-graining procedure applied to the particle population. The standard hierarchy is able to simulate only a narrow range of time- and lengthscales of motion, and this yields errors. The theory presented in this paper broadens the range by replacing fixed internal parameters of the models with randomized parameters specified by their statistical distributions. The parameter distributions are to be found from the standard oceanic observations, or, as in this paper, from fluid-dynamic, eddy-resolving ocean solutions. The practical idea behind the theory is to utilize the kinematic information contained in the observations on a much better level than the common use of the average parameter values.

Here is the summary of the results of this paper (further discussed below):

- 1) The phenomenology of the fluid-dynamic Lagrangian transport is analyzed at very large Re^{18} ;
- 2) the idea of randomized stochastic models is formulated and the new transport properties are illustrated with the first kinematic-time parameter and the Markov-2 model;
- 3) the randomized Markov-2 (RM-2) model is adapted for the inhomogeneous oceanic gyre situation and its solutions are tested against the fluid-dynamic transport;
- 4) the systematic differences between the RM-2 and Markov-2 solutions are analyzed;
- 5) Comparisons are made between the direct RM-2 solutions and the Markov-0, that is, random-walk, solutions with the eddy diffusivity coefficient estimated with the RM-2 model;
- 6) it is shown that all stochastic-model parameters can be estimated locally in space;
- 7) the Lagrangian integral times estimated with the RM-2 model are compared with prior theoretical estimates, and the systematic differences are analyzed;
- 8) a preliminary (and essentially negative) test is made of an empirical closure that relates stochastic-model parameters and large-scale flow properties.

The transport complexity poses the main challenge to simple transport models: the flow is full of transient mesoscale coherent structures, such as swift meandering currents, intense vortices, eddies, and planetary waves, all of which transport the material in a very nondiffusive way; that is, the spreading process described by the single-particle dispersion, $D(t)$, is

¹⁸ The turbulent solution used in this paper is characterized by an Re 5 times as large as in the previous studies of BMB and BM. The flow contains more eddies, and the resulting eddy variability is more realistic.

strongly nonlinear and nonmonotonic. The $D(t)$ is ballistic on short times and predominantly sub- or superdiffusive on intermediate times (up to a few months). The standard stochastic model hierarchy simulates only a narrow range of Lagrangian behaviors as defined by the specific parameter values. This constraint is overcome by introducing randomized, but physically grounded, parameters that represent different contributions from different types of eddies, as expressed in terms of several Lagrangian particles populations with distinct properties. This idea requires an extensive study of various aspects of the models, and this paper reports only a modest advance in this direction. Here, the focus is on the Markov-2 model from the hierarchy, although the theoretical extension to the other members of the hierarchy is straightforward. The Markov-2 model is capable of simulating intermediate-time, subdiffusive spreading processes associated with oscillatory Lagrangian velocity autocorrelation function, $R(\tau)$, that is, with rotary or oscillatory motion of Lagrangian particles in coherent structures. The first kinematic time, $T^{(1)}$, one of the model parameters, contains important information about the spreading process including the subdiffusive behavior: it describes the average rotary motion of Lagrangian particles that occurs when the acceleration and velocity vectors are not aligned with each other. The Markov-2 model with randomized $T^{(1)}$ is referred to as the randomized Markov-2 model. Parameters of the RM-2 model are estimated from the simple statistical properties of the flow, and its performance is tested against the fluid-dynamic solution of the turbulent, passive-tracer transport in oceanic gyres. It is shown that the randomization yields substantially more realistic Lagrangian velocity correlations and dispersion, and it gives relatively good simulations of the gyre transport properties.

The stochastic models can be applied either directly or indirectly; the particular choice depends on the problem itself and the desired accuracy. In the indirect application, the stochastic-model solution is obtained with the locally estimated parameters, and the solution's large-time asymptotic behavior yields the corresponding eddy diffusivity, K . Then, the transport is simulated by the Markov-0 (or, equivalently, advection-diffusion) model with this K . Obviously, the direct approach better accounts for the coherent structures, but also it brings in additional complexity. It is found that the Markov-0 model overestimates (underestimates) the spreading rates when $\beta^{(1)}$, that is, ratio of $T^{(1)}$ and the fading-memory timescale, is small (large). In the fluid-dynamic model, most of the upper-ocean intergyre flux occurs in the western part of the basin, where $\beta^{(1)}$ is relatively small; in the western basin, where $\beta^{(1)}$ is large, the flux is small. Because of this, the Markov-0 model overestimates the mean intergyre fluxes.

A parameter estimation algorithm is proposed that is *local* in space, unlike the traditional approach based on

the large-time asymptotic spreading of the Lagrangian floats. The new stochastic formalism allows for more efficient extraction of the transport information from ocean observations, both Eulerian and from floats. Also, the relatively complex and nonlocal estimating procedure proposed in BM for the fading-memory time parameter is replaced: the fading-memory time is found as the Eulerian envelope-decay time scale of the velocity correlation function. Finally, this study finds no simple closure relationship between the transport parameters and the time-mean currents.

One of the approaches to estimate K is to relate it to a single spreading timescale that is a simple function of basic fluid-dynamic processes, such as baroclinic instability (Visbeck et al. 1997; Stammer 1998). Although this approach is tempting, this paper yields little support of it. It is shown that a lot of information that has direct influence on T_L is hidden in kinematic details of the turbulence and is related to the coherent fluid structures. The high-order stochastic models and their randomized extensions account, to some degree, for the coherent structures and, therefore, provide a more powerful theory than simple scaling laws.

There are many issues that need further investigation before implementing the transport models in coarse-grid GCMs. The physical assumptions (section 1b) of two-dimensional (geostrophic) flow and of tracer adiabaticity can be relaxed by extending the stochastic formalism to the vertical dimension and by including sinks and sources of the tracer. The assumption of the dynamical passiveness is more difficult to relax. Further progress, based on a more detailed analysis of the Eulerian velocity autocorrelation functions, is needed for more precise estimates of the fading-memory time, θ . Perhaps a randomization of θ can improve the model performance. Also, the stochastic transport theory has to be extended to incorporate different distributions of P_u for different values of $T^{(1)}$. Another improvement is to introduce variable-time intervals for the kinematic events. Some other issues arising from the several shortcuts taken here are the following: including nondiagonal terms in the parameter tensors; including large-scale, low-frequency variability (i.e., nonstationarity) in the transport models; examining the nonuniqueness of the drift correction terms; finding more realistic boundary condition for motion of the Lagrangian particles; extending the formalism to account for mixing processes (e.g., as described by the two-particle dispersion); and designing ocean measurement strategies for the parameter estimates.

Acknowledgments. Funding for this research was provided by NSF Grants OCE 96-33681 and OCE 00-91836, and by ONR Grant N00014-98-1-0165. We are grateful for the constructive remarks of the anonymous reviewers.

APPENDIX A

Fluid-Dynamic Model

The midlatitude fluid-dynamic ocean circulation is driven by the asymmetric zonal wind stress:

$$\tau^x(y) = \tau_0 \left\{ \cos \left[\frac{2\pi(y - L/2)}{L} \right] + \epsilon \sin \left[\frac{\pi(y - L/2)}{L} \right] \right\}, \quad (A1)$$

where $\tau_0 = 0.04 \text{ N m}^{-2}$, $L = 3840 \text{ km}$ is the size of the square basin (with $0 \leq y \leq L$), and the forcing asymmetry parameter is $\epsilon = 2$. The basin bottom is flat, and there is no-slip lateral boundary condition for the velocity. The ocean is discretized vertically in three isopycnal layers with depths $H_1 = 200 \text{ m}$, $H_2 = 1200 \text{ m}$, and $H_3 = 2600 \text{ m}$ starting from the top. The ratio of the density jumps across the layer interfaces is $\gamma = (\rho_2 - \rho_1)/(\rho_3 - \rho_2) = 2$, and the first internal Rossby deformation radius is 52 km . The ocean dynamics is QG, and it operates at large Reynolds number,

$$\text{Re} = \frac{UL}{\nu} = \frac{\tau_0}{\rho_1 H_1 \beta \nu}, \quad (A2)$$

where $U = \tau_0(\rho_1 H_1 L \beta)^{-1}$ is the upper-ocean velocity scale derived from the Sverdrup balance; $\beta = 2 \times 10^{-11} \text{ m}^{-1} \text{ s}^{-1}$ is the planetary vorticity gradient; and the lateral viscosity is $\nu = 20 \text{ m}^2 \text{ s}^{-1}$. The Re is about 500. The horizontal grid resolution is uniform with 1025×1025 grid points and 3.75-km intervals between them. In this paper, the presentation is focused on only the upper and middle isopycnal layers because the Lagrangian properties in the bottom and middle layers are qualitatively similar. After the initial spinup process from a state of rest, the solution equilibrates, and then it is computed for 5000 days and stored for the analysis. As the primary evaluation criteria for the transport models the following properties are analyzed: the fluid-dynamic, Lagrangian, meridional, time-average intergyre fluxes^{A1}, and the associated large-scale PDFs of the particle populations.

^{A1} In general, global and single-basin GCMs are intended to simulate the large-scale spreading process and meridional fluxes more than the mesoscale transport properties; therefore, here the former aspects are emphasized, but the ultimate goal is to create skillful transport models that operate equally well on all scales.

$$M_1(P) = 2b \frac{1 + cm^3}{1 + cm^2}, \quad (B1)$$

$$M_2(P) = 2b^2 \frac{1 + c^2m^6 + cm^2(3 - 4m + 3m^2)}{(1 + cm^2)^2}, \quad (B2)$$

$$M_3(P) = 4b^3 \frac{1 + c^3m^9 + 3c^2m^4(2 - 3m + m^2 + m^3) + 3cm^2(1 + m - 3m^2 + 2m^3)}{(1 + cm^2)^3}, \quad (B3)$$

The flow has the following dynamical properties. Instantaneous, upper-ocean circulation has an asymmetric, double-gyre structure with two WBCs and their associated eastward jet extensions and recirculation zones. The robust asymmetry of the gyres is due to the wind forcing asymmetry. The eastward jets strongly meander and occasionally merge (Siegel et al. 2001), therefore the time-mean, upper-ocean velocity streamfunction exhibits broad eastward flow with a moderately strong, single eastward jet separating the gyres (Fig. A1a). The time-mean flow in the deep ocean is relatively weak except near the subtropical WBC and its eastward jet extension where it is predominantly anticyclonic (Fig. A1c). These gross features of the time-mean circulation are preserved at even higher Re (Siegel et al. 2001). In the WBCs intensity of the velocity fluctuations (Figs. A1b,d) is similar to BMB, but in the eastern part of the basin it is larger by factor of 2; hence it is close to the observations (Krauss and Böning 1987). The isotropy of the velocity fluctuations in the interior of the basin decreases with Re from about 2 (BMB) to more realistic values of about 1.4 (here), with enhanced meridional component. All of this suggests that in the larger-Re regime the eddy variability is more realistic.

The fluid-dynamic fluctuations are intense at all depths near the main currents, and typical fluctuation velocities are about 0.5 in the upper and 0.2 m s^{-1} in the deep ocean (Figs. A1b,d). The fluctuations are substantially anisotropic away from the main currents. In the interior of the basin: $\sigma_{22}/\sigma_{11} \approx 2$; and near the lateral boundaries (except the western one) the anisotropy is even larger. The fluctuation properties are qualitatively similar to those in the regime at lower Re (BMB), but here the population of coherent eddies is larger and there are more relatively small-scale features (Siegel et al. 2001).

APPENDIX B

Low-Order Statistical Moments of the Analytical $P(T^{(1)})$

The distribution function (38) contains four parameters that can be found from its first four statistical moments (35). Analytical expressions for the moments are the following:

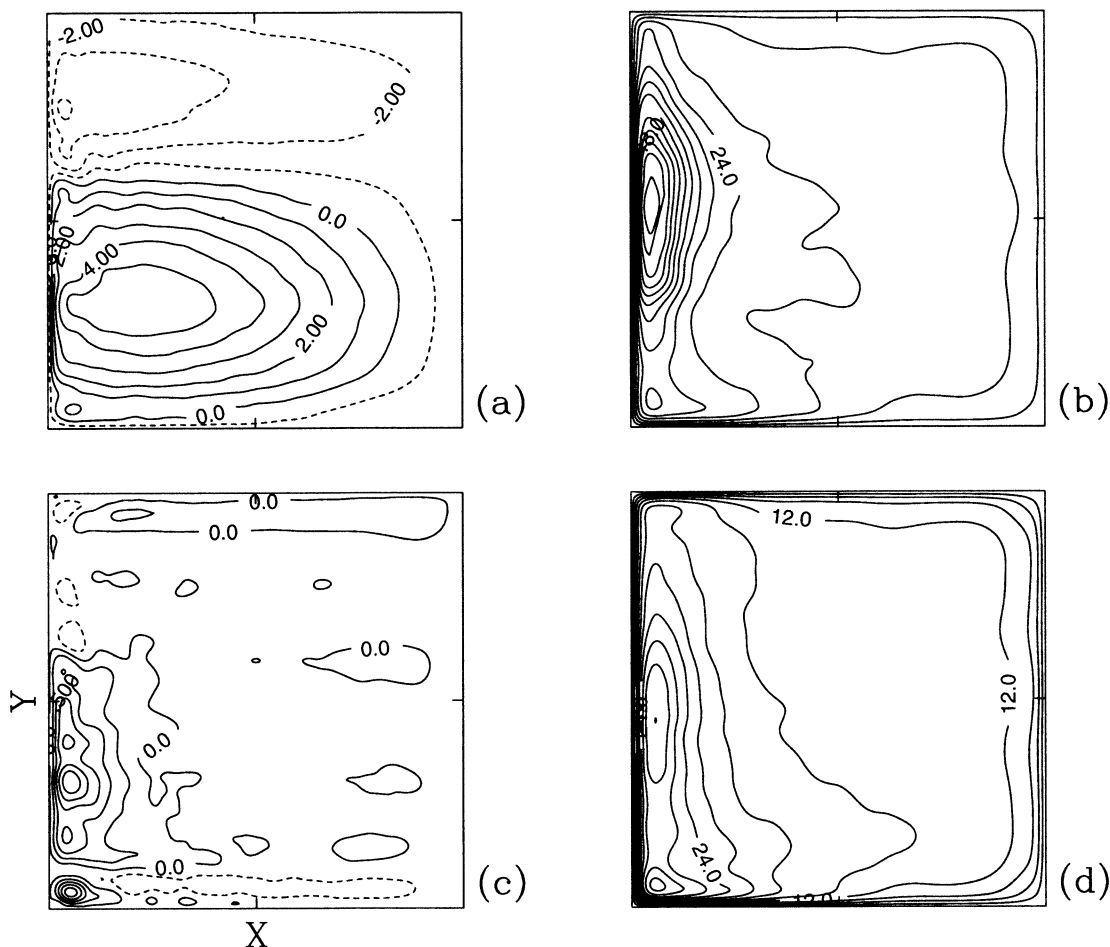


FIG. A1. (a), (c) The time-mean velocity streamfunction and (b), (d) $\sqrt{\sigma_{11} + \sigma_{22}}$ in the (a), (b) upper and (c), (d) deep ocean. Contour intervals: (a) $10^4 \text{ m}^2 \text{ s}^{-1}$, (b) 6.0 cm s^{-1} , (c) $0.25 \times 10^4 \text{ m}^2 \text{ s}^{-1}$, and (d) 3.0 cm s^{-1} .

$$M_4(P) = \frac{24b^4}{(1 + cm^2)^4} [1 + c^4m^{12} + cm^2(5 - 4m + 6m^2 - 8m^3 + 5m^4) + c^3m^6(5 - 8m + 6m^2 - 4m^3 + 5m^4) + c^2m^4(7 - 4m - 4m^3 + 7m^4)]. \quad (\text{B4})$$

APPENDIX C

Markov-0 Model

The governing equation of the Markov-0 model is

$$dx_i = \bar{u}_i(\mathbf{x})dt + \tilde{a}_i^{(0)}(\mathbf{x})dt + b_{ij}^{(0)}(\mathbf{x})dW_j(t), \quad (\text{C1})$$

where the random forcing amplitude is related to the diffusivity coefficient according to

$$b_{ij}^{(0)}b_{jk}^{(0)} = K_{ik} \quad (\text{C2})$$

and the second rhs term in (C1) is the zeroth drift correction, which appears due to inhomogeneities of $K_{ik}(\mathbf{x})$ [superscript (0) is used to indicate the order of the model]. The “well-mixed state” of the tracer is the situation

when the conditional PDF of the Lagrangian tracer, $P_L[t, \mathbf{x} | \mathbf{x}(0)]$, is proportional to the Eulerian PDF, $P_E(t, \mathbf{x})$. The Fokker–Planck equation corresponding to the zeroth-order Markov model is

$$\frac{\partial P}{\partial t} + \frac{\partial(\bar{u}_i P)}{\partial x_i} + \frac{\partial(a_i P)}{\partial x_i} = + \frac{\partial^2}{\partial x_i \partial x_k} \left(\frac{1}{2} b_{ij}^{(0)} b_{jk}^{(0)} P \right). \quad (\text{C3})$$

In the stationary situation ($\partial P / \partial t = 0$), when the tracer is well mixed: $P_E \sim P_L \sim \text{const}$. Hence, from (C3) it follows that

$$a_i^{(0)} = \frac{\partial}{\partial x_k} \left[\frac{1}{2} b_{ij}^{(0)} b_{jk}^{(0)} \right] \quad (\text{C4})$$

(the constant of integration is zero because there is no

average drift of particles in the homogeneous situation), and finally with (C2) we obtain

$$a_i^{(0)} = \frac{1}{2} \frac{\partial K_{ik}}{\partial x_k}. \quad (\text{C5})$$

By substituting (C5) in (C3), one gets the final form of the Fokker–Planck equation:

$$\frac{\partial P}{\partial t} + \bar{u}_i \frac{\partial P}{\partial x_i} = \frac{1}{2} \frac{\partial}{\partial x_i} \left(K_{ik} \frac{\partial P}{\partial x_k} \right). \quad (\text{C6})$$

REFERENCES

- Babiano, A., C. Basdevant, P. Le Roy, and R. Sadourny, 1987: Single-particle dispersion, Lagrangian structure function and Lagrangian energy spectrum in two-dimensional incompressible turbulence. *J. Mar. Res.*, **45**, 107–131.
- Berloff, P., and J. McWilliams, 1999a: Large-scale, low-frequency variability in wind-driven ocean gyres. *J. Phys. Oceanogr.*, **29**, 1925–1949.
- , and —, 1999b: Quasigeostrophic dynamics of the western boundary current. *J. Phys. Oceanogr.*, **29**, 2607–2634.
- , and —, 2002: Material transport in oceanic gyres. Part II: Hierarchy of stochastic models. *J. Phys. Oceanogr.*, **32**, 797–830.
- , —, and A. Bracco, 2002: Material transport in oceanic gyres. Part I: Phenomenology. *J. Phys. Oceanogr.*, **32**, 764–796.
- Borgas, M., and B. Sawford, 1994: Stochastic equations with multifractal random increments for modeling turbulent dispersion. *Phys. Fluids*, **6**, 618–633.
- , T. Flesch, and B. Sawford, 1997: Turbulent dispersion with broken reflectional symmetry. *J. Fluid Mech.*, **332**, 141–156.
- Bower, A., and S. Lozier, 1994: A closer look at particle exchange in the Gulf Stream. *J. Phys. Oceanogr.*, **24**, 1399–1418.
- Box, G., G. Jenkins, and G. Reinsel, 1994: *Time Series Analysis: Forecasting and Control*. Prentice Hall, 598 pp.
- Bracco, A., J. LaCasce, and A. Provenzale, 2000: Velocity pdfs for oceanic floats. *J. Phys. Oceanogr.*, **30**, 461–474.
- Colin de Verdiere, A., 1983: Lagrangian eddy statistics from surface drifters in the eastern North Atlantic. *J. Mar. Res.*, **41**, 375–398.
- Davis, R., 1987: Modeling eddy transport of passive tracers. *J. Mar. Res.*, **45**, 635–666.
- Figuerola, H., 1994: Eddy resolution versus eddy diffusion in a double gyre GCM. Part II: Mixing of passive tracers. *J. Phys. Oceanogr.*, **24**, 387–402.
- , and D. Olson, 1994: Eddy resolution versus eddy diffusion in a double gyre GCM. Part I: The Lagrangian and Eulerian description. *J. Phys. Oceanogr.*, **24**, 371–386.
- Freeland, H., P. Rhines, and T. Rossby, 1975: Statistical observations of the trajectories of neutrally buoyant floats in the North Atlantic. *J. Mar. Res.*, **33**, 383–404.
- Gardiner, C., 1983: *Handbook of Stochastic Processes for Physics, Chemistry and the Natural Sciences*. Springer-Verlag, 442 pp.
- Griffa, A., 1996: Applications of stochastic particle models to oceanographic problems. *Stochastic Modelling in Physical Oceanography*, R. Adler et al., Eds., Birkhauser, 467 pp.
- , K. Owens, L. Piterbarg, and B. Rozovskii, 1995: Estimates of turbulence parameters from Lagrangian data using a stochastic particle model. *J. Mar. Res.*, **53**, 371–401.
- Jiang, S., F. Jin, and M. Ghil, 1995: Multiple equilibria, periodic, and aperiodic solutions in a wind-driven, double-gyre, shallow-water model. *J. Phys. Oceanogr.*, **25**, 764–786.
- Kaneda, Y., T. Ishihara, and K. Gotoh, 1999: Taylor expansions in powers of time of Lagrangian and Eulerian two-point two-time velocity correlations in turbulence. *Phys. Fluids*, **11**, 2154–2166.
- Karlin, S., and H. Taylor, 1975: *A first course in stochastic processes*. Academic Press, 557 pp.
- Krauss, W., and C. Böning, 1987: Lagrangian properties of eddy fields in the northern North Atlantic as deduced from satellite-tracked buoys. *J. Mar. Res.*, **45**, 259–291.
- LaCasce, J., and A. Bower, 2000: Relative dispersion in the subsurface North Atlantic. *J. Mar. Res.*, **58**, 863–894.
- Luhar, A., M. Hibberd, and P. Hurley, 1996: Comparison of closure schemes used to specify the velocity PDF in Lagrangian stochastic dispersion models for convective conditions. *Atmos. Environ.*, **30**, 1407–1418.
- Lumpkin, R., and P. Flament, 2001: Lagrangian statistics in the central North Pacific. *J. Mar. Syst.*, **29**, 141–155.
- , A.-M. Treguier, and K. Speer, 2002: Lagrangian eddy scales in the northern Atlantic Ocean. *J. Phys. Oceanogr.*, **32**, 2425–2440.
- Maurizi, A., and S. Lorenzani, 2001: Lagrangian time-scales in homogeneous non-Gaussian turbulence. *Flow, Turb. Combust.*, **67**, 205–216.
- Pasquero, C., A. Provenzale, and A. Babiano, 2001: Parameterization of dispersion in two-dimensional turbulence. *J. Fluid Mech.*, **439**, 279–303.
- Piterbarg, L., 2001: The top Lyapunov exponent for a stochastic flow modeling the upper ocean turbulence. *SIAM Appl. Math.*, **62**, 777–800.
- Pope, S., 1994: Lagrangian PDF methods for turbulent flows. *Annu. Rev. Fluid Mech.*, **26**, 23–63.
- Reynolds, A., 2002: On Lagrangian stochastic modelling of material transport in oceanic gyres. *Physica D*, **172**, 124–138.
- Risken, H., 1989: *The Fokker–Planck Equation*. Springer-Verlag, 472 pp.
- Roberts, M., and D. Marshall, 2000: On the validity of downgradient eddy closures in ocean models. *J. Geophys. Res.*, **105**, 28 613–28 627.
- Rodean, H., 1996: *Stochastic Lagrangian Models of Turbulent Diffusion*. Amer. Meteor. Soc., 79 pp.
- Rupolo, V., B. Hua, A. Provenzale, and V. Artale, 1996: Lagrangian velocity spectra at 700 m in the western North Atlantic. *J. Phys. Oceanogr.*, **26**, 1591–1607.
- Sawford, B., 1991: Reynolds number effects in Lagrangian stochastic models of turbulent dispersion. *Phys. Fluids A*, **3**, 1577–1586.
- Siegel, A., J. Weiss, J. Toomre, J. McWilliams, P. Berloff, and I. Yavneh, 2001: Eddies and vortices in ocean basin dynamics. *Geophys. Res. Lett.*, **28**, 3183–3187.
- Smagorinsky, J., 1993: Some historical remarks on the use of nonlinear viscosities. *Large Eddy Simulation of Complex Engineering and Geophysical Flows*, B. Galperin and S. Orszag Eds., Cambridge University Press, 3–36.
- Stammer, D., 1998: On eddy characteristics, eddy transports, and mean flow properties. *J. Phys. Oceanogr.*, **28**, 727–739.
- Taylor, G., 1921: Diffusion by continuous movement. *Proc. London Math. Soc.*, **20**, 196–212.
- Thomson, D., 1987: Criteria for the selection of stochastic models of particle trajectories in turbulent flows. *J. Fluid Mech.*, **180**, 529–556.
- Visbeck, M., J. Marshall, T. Haine, and M. Spall, 1997: Specification of eddy transfer coefficients in coarse-resolution ocean circulation models. *J. Phys. Oceanogr.*, **27**, 381–402.